Copyright © 2002, by the author(s).
All rights reserved.

Permission to make digital or hard copies of all or part of this work for personal or classroom use is granted without fee provided that copies are not made or distributed for profit or commercial advantage and that copies bear this notice and the full citation on the first page. To copy otherwise, to republish, to post on servers or to redistribute to lists, requires prior specific permission.

COULOMB INTERACTIONS IN HIGH THROUGHPUT ELECTRON BEAM LITHOGRAPHY

by

Bo Wu

Memorandum No. UCB/ERL M02/4

26 February 2002

COULOMB INTERACTIONS IN HIGH THROUGHPUT ELECTRON BEAM LITHOGRAPHY

by

Bo Wu

Memorandum No. UCB/ERL M02/4

26 February 2002

ELECTRONICS RESEARCH LABORATORY

College of Engineering
University of California, Berkeley
94720

Coulomb Interactions in High Throughput Electron Beam Lithography

by

Bo Wu

B.A. (University of Rochester) 1992
M.S. (University of Michigan, Ann Arbor) 1994

A dissertation submitted in partial satisfaction of the

requirements for the degree of

Doctor of Philosophy
in

Physics

in the

GRADUATE DIVISION

of the

University of California at Berkeley

Committee in charge

Professor Andrew R. Neureuther, Chair
Professor Jonathan Wurtele, Cochair
Professor W. Oldham
Professor Roger Felcone

Spring 2002

The dissertation of Bo Wu is approved:

Chair | Date

Cochair | Date

Date

Date

University of California, Berkeley

Spring 2002

Coulomb Interactions in High Throughput Electron Beam Lithography

Copyright 2002

by

Bo Wu

Abstract

Coulomb Interactions in High Throughput Electron Beam Lithography

by

Bo Wu

Doctor of Philosophy in Physics

University of California at Berkeley

Professor Andrew R. Neureuther, Chair

Professor Jonathan Wurtele, Cochair

High throughput electron beam lithography systems have been viewed as promising candidates for sub-100nm wafer writing tools. This thesis extends previous work in the study of electron Coulomb interactions and the study of electron interactions with photo-resists. Both of these interactions contribute to image blur and the studies in this thesis provide physical insight, quantitative characterization and suggest methods of reducing blur.

The Berkeley Electron Beam Simulator (BEBS) is a collection of software tools developed by the author to study the charged particle interactions in beam columns. BEBS employs the Fast Multi-pole Method (FMM) for rigorous force calculations. It takes about one hour with ten 500MHz processors to simulate a 30μA beam current in a typical 4× demagnification system using a packet of 13,000 particles. The accuracy of the force calculation algorithm is benchmarked with that of Munro's electron beam simulator. BEBS provides many options for observing forces and trajectory changes, and improving beam spot size. These options have been successfully applied and proved especially useful in studying stochastic interactions affecting beam blur.

The influence of space charge on the electron dynamics is investigated with simulations. The primary consequence of space charge is beam blur. Beam blur reduction techniques are examined using both neutralizing ions and lens aberrations. Results show that around *80%* of the space charge blur is eliminated at $30\mu A$ beam current and that the total beam blur is reduced by nearly 30%. Further beam blur reduction would be formidable unless the stochastic blur is also reduced.

The basic assumptions of Mkrtchyan's Nearest Neighbor Theory are tested. It is demonstrated that for typical e-beam lithography applications, electron interaction with multiple neighbors rather than the nearest neighbors is the norm other than exception in a typical electron beam system. The simulation shows that the randomized correlation length is a function of the beam diameter and that correlated interactions occur at other axial positions due to symmetry with respect to the beam crossover. The structures of stochastic Coulomb interactions have been analyzed in probe-forming systems through a novel approach that combines algebraic analysis of forces and simulation of relocated trajectory displacements. This approach is able to explain why a crossover beam and a homocentric parallel beam with the same beam angle produce the same beam blur in spite of the high electron densities that occur in the crossover case.

Scaling laws for stochastic blur are developed. In a beam projection or multi-emitter array system, the stochastic blur is proportional to beam current raised to the power of 0.62, which roughly agrees with Jansen's prediction of 0.67. The scaling laws of the stochastic blur are also formulated with respect to column length, beam convergence angle, emitter spacing and beam voltage.

Professor Andrew R. Neureuther

Dissertation Committee Chair

Professor Jonathan Wurtele

Dissertation Committee Cochair

Table of Contents

CHAPTER 1. Introduction 1

1.0 Tools 1
1.1 Thesis 2
1.2 Academic contributions 4

CHAPTER 2. Background 8

2.0 Challenges 8
2.1 Stochastic effect 9
2.2 Space charge effect 10
2.3 Simulation tools 11
2.4 Electron-resist interactions 13

CHAPTER 3. Beam Electron Beam Simulator – algorithms and characteristics 15

3.0 Introduction 15
3.1 Force computations in BEBS 15
3.1.0 Pbody library 15
3.1.1 Electron bunch 17
3.1.2 Lorentz transformations 18
3.2 Time iteration 20
3.3 Post-processing of data 23
3.4 Special options in BEBS 25
3.5 Comparison with Munro's Software 27
3.5.1 Barnes-Hut algorithm 27
3.5.2 Accuracy and speed comparison 28

CHAPTER 4. Beam Blur Contributions in Multi-emitter Array Systems 34

4.0 Introduction 34
4.1 Blur contribution along the optical axis 34
4.2 Inter-beamlet, intra-beamlet electron interactions and the summation rule 39
4.2.0 Mask configurations 39
4.2.1 Summation rule for beam blur contributions 40
4.2.2 Inter-beamlet and intra-beamlet blur contributions 41
4.2.3 Inter-beamlet blur contribution and emitter spacing on the mask 43
4.3 Conclusions 46

CHAPTER 5. Stochastic Coulomb Interactions and Neighboring Electrons 47

5.0 Introduction 47
5.1 System setup 47

5.2 Numbers of neighboring electrons 49
5.3 Effect of neighboring electrons upon the transverse forces......... 52
5.4 Conclusions... 55

CHAPTER 6. Structure Of Stochastic Coulomb Interactions............... 56

6.0 Introduction... 56
6.1 Stochastic interactions in a probe-forming beam with a crossover 58
6.1.0 Stochastic force upon a single electron.............................. 58
6.1.1 Averaged stochastic force... 60
6.1.2 Blur contribution along the optical axis.............................. 64
6.2 Stochastic interactions in a homocentric parallel beam.............. 69
6.3 Other probe forming beam configurations.............................. 72
6.4 Stochastic interactions in a system with multi-emitter array........ 73
6.5 Conclusions... 75

CHAPTER 7. Scaling Laws for Stochastic Coulomb Interactions............ 76

7.0 Introduction... 76
7.1 Theory... 78
7.2 Scaling laws... 80
7.2.0 Comparison with Jansen's Theory.................................... 80
7.2.1 Scaling laws for a 25-emitter array system 81

CHAPTER 8. Impact of Positive Ions and Effect of Lens Aberrations...... 86

8.0 Introduction... 86
8.1 Impact of positive ions.. 87
8.2 Effect of lens aberrations... 92
8.3 Summary and conclusions.. 95

CHAPTER 9. Electron Interaction with Photo-resist.......................... 96

9.0 Introduction... 96
9.1 Schematics of ERIM.. 97
9.2 Secondary electron emission process................................ 99
9.3 Exposure process... 102
9.4 Spatial profile of exposure events.................................... 105
9.5 Exposure dose.. 106
9.6 Conclusions and discussion... 107

CHAPTER 10. Conclusions... 110

10.0 Numerical and analytical tools...................................... 110
10.1 Mechanism studies and beam blur reductions........................ 111
10.2 Future work... 114

Bibliography... 117

Acknowledgements

I would like to thank my advisor, Professor Andrew R. Neureuther for helping me make this transition to application oriented research. Without his guidance and support, I would not have been able to complete my thesis project within three years. He is a role model for me with his enthusiasm, diligence, and uncompromising standards.

I would like to thank my physics co-advisor, Professor Jonathan Wurtele, for his consistent support. His insight and outlook as a physicist makes my thesis a physics one. Thanks are due to Professor Roger Falcone, former Chair of the physics department, for his understanding and steady support. I would also like to thank Professor William Oldham for serving on my qualifying and thesis committees. I am grateful to Professor Wulf Kunkel for serving on my qualifying committee.

I had the good fortune of working with my colleagues and friends, Dr. Mosong Cheng, Dr. Ebo Croffie, Lei Yuan, Michael Williamson, Yunfei Deng, Yashesh Shroff, Mr. Junwei Bao, Yijian Chen, Jason Cain, Garth Robins, Dr. Liqun Han and Dr. Gil Vinograd for their friendship to support. Mosong and Ebo were especially helpful during the initial stage of this research project. They helped me more than they probably ever realized.

I would like to thank my immediate and extended families for their support throughout my education. Last but not least, I thank the Lord for answering my prayers and for helping me all the way through this incredible journey.

1 Introduction

High throughput electron beam systems, such as SCALPEL [1] and PREVEAIL [2], have been used as potential candidates for sub-100nm lithographic tools. The ultimate resolution in high throughput electron beam lithography is strongly limited by the electron-electron interactions in the beam column [3] [4] and the electron interactions with photo-resist [5]. A thorough understanding of these interactions is vital to the design of any high throughput electron beam systems.

1.0. Thesis

The contents of this thesis are classified into two categories: (a) analytical and simulation tools, including the characteristics of the Berkeley Electron Beam Simulator (BEBS) developed by this author and its algorithms, and (b) scientific contributions in the study of electron interactions in beam columns and the study of electron interaction with photo-resist. This chapter highlights the thesis contribution and provides a few key references. The general background is provided in Chapter 2 with more complete references.

1.1. Tools

Experimenting with high throughput electron beam systems is very costly and time consuming. System modeling gives insight to the physical mechanisms and provides general guidelines for the design. A large number of theoretical works have been dedicated to the study of the electron stochastic interactions [6] [7] and the global space charge effect [3] in electron beam columns. Among these, simulation techniques provide a powerful tool for the study of the collective behavior of a large number of charged particles in the beam column. All the beam and column parameters can be easily tuned in simulations. The simulation approach is particularly useful in the study of the electron stochastic blurs when the analytical approach is formidable.

A serious drawback of some existing electron beam simulators is that the computation time is proportional to the square of number of electrons, which makes the high beam current simulation intractable. Munro *et al.* have been developing commercial software for the design of electron beam lithographic systems [8] [9]. Since the initiation of this thesis work, Munro uses the Barnes-Hut method [10] in his commercial electron beam simulator to reduce the amount of computation required [11]. A detailed comparison between BEBS and Munro's simulator is provided in Section 3.6 of this thesis. Han and Winograd [12] [13] developed an electron beam simulator at Stanford University to study the global space charge effect. Its force computations, however, are based on an unverified approximation of "test" electrons and "field" electrons.

The force computations in the BEBS are performed with Pbody [14] [15], which is a parallel library running on multiple processors. It employs the Fast Multipole Method (FMM) [16] [17] for fast and rigorous force calculations. The computation time is roughly proportional to the number of electrons and inversely proportional to the number of processors.

Compared with other existing electron beam simulators, BEBS provides a number of special options for the study of beam blur production mechanisms. These options include identifying the neighboring electrons of an arbitrary electron of concern, directly generating stochastic blurs in simulations through the use of positrons, etc. Each option has been successfully applied in the academic contributions of this thesis. Chapter 3 will discuss the details of BEBS' computational algorithms and special options.

Facing many body problems, analytical approaches often lead to algebraic expressions that are not solvable. Simulation techniques avoid this problem. Yet, the underlying physical principles may be hidden. To address these shortcomings, the author developed an approach [18] which combines analytical approach and simulation technique and uses the strength of both. This new approach is successfully applied to the study of the structure of electron stochastic interactions in Chapter 6.

Some early work on electron-resist interactions owes to Greeneich [19] [20] and Shimizu [21] on the modeling of electron-resist interaction. In 1980's Murata *et al.* [22] [23] developed the hybrid model to study energy deposition in photo-resist. Murata's

model, however, is based on the assumption that all forms of deposited energy contribute equally to the exposure events and the detailed mechanisms of exposure reactions were not considered.

The Electron-Resist Interaction Model (ERIM) presented in Chapter 9 of this thesis is the first of its kind to study the electron resist interaction mechanisms using reaction cross sections [24]. ERIM is a pure analytical model, which gives an algebraic expression for the spatial distribution of exposure events.

1.2. Academic contributions

This thesis first examines the beam blur contributions in terms of axial positions, and inter- and intra-beamlet electron interactions [25]. The results are presented in Chapter 4. The chapter also presents the summation rule of inter- and intra-beamlet interactions.

The electron statistical interactions create image blurs that are not correctable through conventional optical system compensation. Theorists developed different models to predict the beam blur caused by the electron-electron stochastic interactions in various beam configurations. Mkrtchyan [6] formulated an analytical model based on the nearest-neighbor approximation. Jansen [7] [26] developed the Extended Two-Particle model for high throughput electron beam systems. Both model also require a series of approximations and untested assumptions.

In Chapter 5 of this thesis, the nearest-neighbor assumption of Mkrtchyan's is tested via simulations. Analysis of a basic crossover showed that interactions with multiple rather than nearest-neighbor electrons almost immediately became the norm rather than the exception.

Jansen's Extended Two-Particle model predicts that a crossover beam and a homocentric parallel beam can produce the same beam blur as long as they share the same beam angle [27]. However, the physical insight is completely buried in the mathematical complexity of his analysis.

Chapter 6 of this thesis provides physical insight and quantitative explanation of Jansen's above prediction. The chapter reveals the rich structures of stochastic interactions in different beam geometries [18], which can be further explored for possible beam blur reduction.

Chapter 7 presents a stochastic effect simulator, which is the first of its kind to produce stochastic blur directly in simulation. It is effectively used to develop the scaling laws for the stochastic blur and the scaling laws for the space charge blur. The chapter also provides the theoretical foundation for the stochastic effect simulator.

Han and Winograd [3] [12] demonstrated that the aberrations induced by the lensing action of global space charge of the electrons result in beam blur that increases with beam current. The space charge effect seriously limits the performance of high

throughput electron beam lithography systems. It was demonstrated in experiments that the spherical aberrations of a focused ion beam can be corrected via electron clouds [28] [29]. However, it was not clear whether the neutralization scheme would be applicable for a high throughput e-beam lithography system due to the scattering of small–mass electrons. Xiu [30] [31] studied the effect of space charge coils and a multi-pole projector in electron beam columns and tried to reduce field curvature and on-axis aberrations. Nevertheless, no quantitative results have been given on beam blur reductions.

Chapter 8 of this thesis discusses the impact of positive ions in beam columns and the effect of lens aberrations as potential techniques to reduce space charge blurs. Results demonstrate that total beam blur can be considerably reduced with either technique in high throughput electron beam systems [32].

The hybrid model developed by Murata [22] is a Monte Carlo program used to simulate the exposure profile of e-beam resist. This model, however, is based on the assumption that all forms of deposited energy contribute equally to the exposure events, which has no physical basis. The exposure mechanisms are beyond the scope of Murata's model.

Chapter 9 of this thesis examines the mechanisms of electron-resist interactions. The chapter reveals the parameter dependencies of the minimum exposure dose and the roles of secondary electrons with the ERIM model [24]. The author derives an analytical

expression for the spatial distribution of exposure events, which is suitable for numerical solution.

2 Background

High throughput electron beam lithography systems are viewed as promising candidates for the next generation of wafer writing tools. In contrast to optical lithography, the resolution of electron beam lithography is no longer limited by wavelength. Several different types of high throughput electron beam systems have been proposed or developed with the goal of producing sub-100nm wafer-writing tools. In a projection electron beam system, such as SCALPEL [1] and PREVAIL [2], developed by Lucent and IBM, respectively, the mask is flood-illuminated by a beam of electrons, and the image is projected on the surface of the wafer. In a multiple emitter array system, each individual emitter can be tuned on or off and patterns on the emitter array are projected onto the wafer.

2.0. Challenges

The disadvantage of electron beam lithography is that the demands for high resolution and high throughput are contradictory due to the repelling forces between electrons in the beam column [33] [34]. Meanwhile, the interaction of an electron beam with photo-resist films produces a spatial distribution of exposure reactions, which imposes another limitation to the resolution of electron beam lithography [35] [36].

Numerous efforts have been made to reduce beam blur at high beam currents to meet a given resolution and throughput requirement.

2.1. Stochastic effect

The electron statistical interactions create image blur that is not correctable through conventional optical system compensation. Different theoretical models have been developed to predict the beam blur caused by the electron-electron stochastic interactions. Berger *et al.* tried to investigate the trajectory displacement effects using Monte Carlo methods [33]. However, the stochastic effect is always convoluted with the space charge effect in his studies. The stochastic effect was never isolated. Weidenhausen *et al.* first introduced the nearest-neighbor (N-N) approach to study the electron stochastic effect in probe-forming systems [37] [38]. Based on the N-N approach, Mkrtchyan *et al.* developed a new model to examine the stochastic interactions in high throughput e-beam systems [6] [39]. Both models are based on consideration of the nearest-neighbor electrons and on the concept of a randomized length, over which interactions are correlated. Mkrtchyan was then able to get agreement with the limited experimental data for a wide range of beam currents. Meanwhile, Van Leeuwen and Jansen proposed the Multiple Independent Collision Approach (MICA) for probe-forming systems [40]. To isolate the stochastic effects the model only considers the collisions of the electrons on the trajectory that runs through the center of a circular beam. Jansen refined the above approach and developed the extended two-particle model for projection e-beam systems [7]. Jansen's model still requires either a first order approximation or a strong- single-collision approximation. Jansen predicts that a

crossover beam and a homocentric parallel beam produce the same beam blur as long as they share the same beam angle [27]. This prediction was later confirmed in simulation results by Brodie *et al.* [41] and Han [42]. Nevertheless, the sophisticated mathematical formulation of his model failed to give convincing physical insight into this problem and the structure of electron stochastic interactions remains hidden.

2.2. Space charge effect

The aberrations induced by the lensing action of global space charge of the electrons also result in beam blur that increases with beam current. Han and Winograd [3][12] have demonstrated through simulations that the allowable current in a high throughput electron beam projection system is strongly limited by these aberrations. In particular, beam-induced space curvature and astigmatism have been recognized as the major contributors to the beam blur. The space charge effect was later observed and studied in the SCAPEL system [43] [44].

Techniques that effectively reduce the space charge effect are vital to the realization of high throughput electron beam lithography tools. The space charge neutralization of electron beams using positive ions has been investigated since 1920's when cathode ray tube was a main focus of the study [45] [46]. In the mid 20th century, topics which involved neutralization were beam transport phenomena, plasma physics and elementary particle physics. The space charge neutralization of ion beams using electrons was demonstrated [47]. In 1997 Chao [28] *et al.* and Orloff [29] show that the

spherical aberrations in ion beams can be corrected via electron clouds. However, it was not clear whether the neutralization scheme would be applicable for a high throughput e-beam system due to the scattering of electrons. Xiu [30] [31] later studied the impact of space charge coils and a multi-pole projector in electron beam systems trying to reduce the field curvature the other space charge induced aberrations in the SCALPEL system. Nevertheless, no quantitative results have been given on beam blur reductions.

2.3. Simulation tool

Simulation techniques serve as a powerful tool for the study of electron Coulomb interactions in the beam column. It is particularly useful in the study of the electron stochastic blur when the analytical approach is formidable. In comparison with experimental techniques, all the beam and column parameters can be easily tuned in simulations.

The largest computational obstacle in the simulation of electron beams is the calculation of the forces exerted on each electron by the other electrons. Calculating this directly is prohibitively time consuming as the computation time grows as the square of the number of particles. A great deal of literature has been devoted to the study of reducing the amount of computation time by allowing the use of approximations. For calculations where high accuracy is not essential, the method of Barnes and Hut [10] is a possible choice, which is used in Munro's commercial electron beam simulation software [11]. The amount of work required by the Barnes-Hut method to perform the force calculation for N particles is proportional to $N \log N$.

Jansen developed the Fast Monte Carlo Simulation (FMCS), which combine the Monte Carlo approach with his Extended Two-particle theory [48]. The accuracy of the simulation, however, is limited by the unverified assumptions and approximations in Jansen's theory. Moreover, the detailed mechanisms of electron-electron interactions can no longer be examined due to these approximations.

The Stanford electron beam simulator, uses "field electrons" and "test electrons" to avoid the large amount of calculations [12] [13]. In this model, all the field electrons follow completely straight trajectories and only provide background electric field for the test electrons. This approximation tends to overestimate the effect of Coulomb interactions in the column. The simulator was mainly used for the study of global space charge effect in beam projection systems.

For simulations that require more accuracy, the Fast Multipole Method (FMM) of Greegard, Carrier and Rokhin [16] is an appropriate choice. Here the amount of work required to perform the calculation is proportional to the number of particles. For a high level of accuracy, it is more efficient than the Barnes-Hut algorithm. Carmichael [49] and Wen *at al.* [50] employs a fully rigorous Fast Multipole Method (FMM) using the DPMTA code from Duke [51] to perform the force calculations for his electron beam simulator. Wen's implementation of FMM does not include local refinement in spatial divisions, which limits its efficiency for highly non-uniform electron distributions, such as a crossover beam.

2.4. Electron-resist interactions

In 1968 Reimer published the single scattering Monte Carlo model [52], in which electron scatterings in solids are simplified by separating the effects of elastic and inelastic scattering events. The angular deflection of an electron is determined by the elastic scattering based on the Rutherford cross section and the energy loss between scatterings is calculated by the continuous slowing down approximation of the Bethe law [53]. The single scattering model has been refined by Reimer *et al.* [54], Curgenven and Duncumb [55], Murata *el al.* [56]. Based on these past studies the Monte Carlo simulation with single scattering was applied to fundamentals of electron beam lithography. The reports by Shimizu and Everhart [21] and Shimizu *et al.* [57] were concerned with energy deposition in bulk PMMA targets. Nevertheless, the single scattering model does not include inelastic collisions or secondary electron productions, which cause spreading of energy absorption.

Based on the single scattering model, Murata *et al.* [22] [58] later developed a hybrid model for lithography applications, which includes discrete energy processes and fast secondary electron productions. The hybrid model provides the profile for the electron energy deposited in the photo-resists. Vriens cross section [59] and the modified Bethe formula by Joy and Luo [60] were used to describe the discrete energy processes. Both models, however, are based on the assumption that all forms of deposited energy contribute equally to the exposure events, which has no physical basis. The detailed mechanisms of exposure reactions are beyond the scope of these models.

In 1992 Lutwyche [61] proposed a semi-classical model to study the resolution of e-beam lithography. G. Han and F. Cerrina [62] later developed an analytical model based on the theory of virtual quanta. In these models, all the exposure events were attributed to the high energy primary electrons. The impact of secondary electrons was not included in the discussions. Moreover, they use overly simplified models for the resist molecules, which overlooks most of the exposure mechanisms.

3 Berkeley Electron Beam Simulator - Algorithms and Characteristics

3.0. Introduction

The Berkeley Electron Beam Simulator (BEBS) is a collection of software tools developed by the author to study the electron Coulomb interactions in beam columns. This chapter discusses the force computations in BEBS in section 3.1. The time iteration algorithm is presented in Section 3.2. Section 3.3 addresses the issue of post-processing of data. Section 3.4 presents BEBS' special options for mechanism studies. Section 3.5 gives a comparison is given between BEBS and Munro's simulation software.

3.1. Force computations in BEBS

3.1.0. Pbody library

The force computations in BEBS are performed with the Pbody library, which is a parallel adaptive N-body solver developed by Blackston and Demmel [14] [15]. Pbody employs a novel locally refinable Fast Multipole Method (FMM) [16] to achieve high efficiency and accuracy. FMM reduces the amount of computation by using spherical harmonics to approximate the effects of sets of particles rather than resorting to direct calculation. The computation time is roughly proportional to the number of charge

particles, and inversely proportional to the number of processors, which is usually between two to fifteen. Currently Pbody is available on two clusters: the *NOW* (Network of Workstations) [63] and the *Millennium* [64] both at UC Berkeley.

The performance of Pbody depends on the settings of four parameters: expansion size *P*, *MAXBN*, *SEPARATION*, and the use of *supernodes* [65]. Pbody includes up to 5th order terms in its spherical harmonics expansions, namely *P=5*. To improve the efficiency of the code, Pbody uses an adaptive approach where the regions that are populated more densely by particles are subdivided more finely cells. Figure 3-1 is a schematic diagram for cell divisions with at most two particles in each cell. In e-beam applications, typically, each cell holds up to *MAXBN=50* particles. A large *MAXBN* results in higher accuracy at the expense of run time. Pbody directly calculates the Coulomb forces for each pair of electrons that belong to the same cell or adjacent cells. These direct calculations become particularly important when the neighboring particles are from different cells [66]. *SEPARATION* is a parameter defined in Pbody to extend the direct calculation zone beyond adjacent cells [67] to produce a more accurate result. *SEPARATION=2* is chosen for BEBS. Pbody allows the use of supernodes, first described by Zhao [68] to reduce the amount of computation with only a small cost in accuracy. A typical 30μA current simulation (~13,000 particles) in a 40cm long column takes about one hour with ten 500MHz processors. Please refer to reference [15] for a more detailed discussion of the Pbody library. A background introduction to FMM used in the simulation of e-beam can be found in Chapter 2.

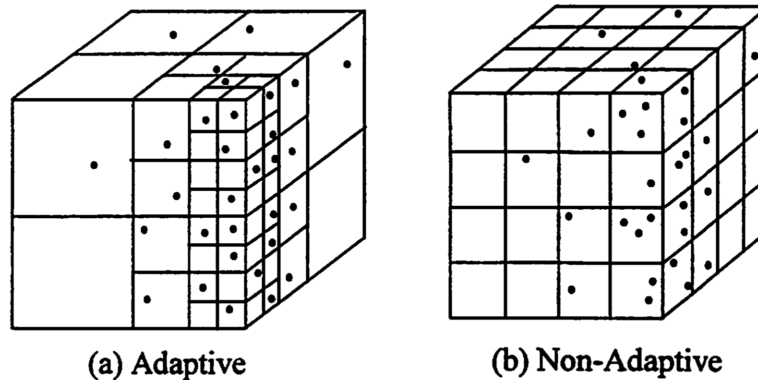

Figure 3-1. The adaptive and the non-adaptive Division of space in FMM.

3.1.1. Electron bunch

Instead of filling the entire simulation column with electrons, BEBS uses single or multiple electron bunches to reduce the computation time. Each electron bunch is 12mm long. In order to avoid the "tail" effect, only the 4mm part in the middle is used to produce image on the target plane as shown Figure 3-2. This method is discussed in reference [13] [69] and is used both by Munro's simulation software and by the Stanford simulator. The projection lenses, whose focal lengths are independent of electron energy, provide a means of directly observing beam blur due to electron-electron Coulomb interactions. These achromatic imaging lenses are appropriate for investigating effects in electron beam lithography systems where the space charge effect and the stochastic effect are expected to dominate image quality such as in SCALPEL.

3.1.2. Lorentz transformations

At beam voltage of 50KV or above, the electron repulsions obey Coulomb's Law only in the center of mass (CM) frame of the electrons due to relativistic effects. Thus, all the electron positions are transformed from the lab frame into the CM frame before the Pbody library can be used. The flowchart of the algorithm is shown in Figure 3-3. Assume that the beam current is in the *z* direction.

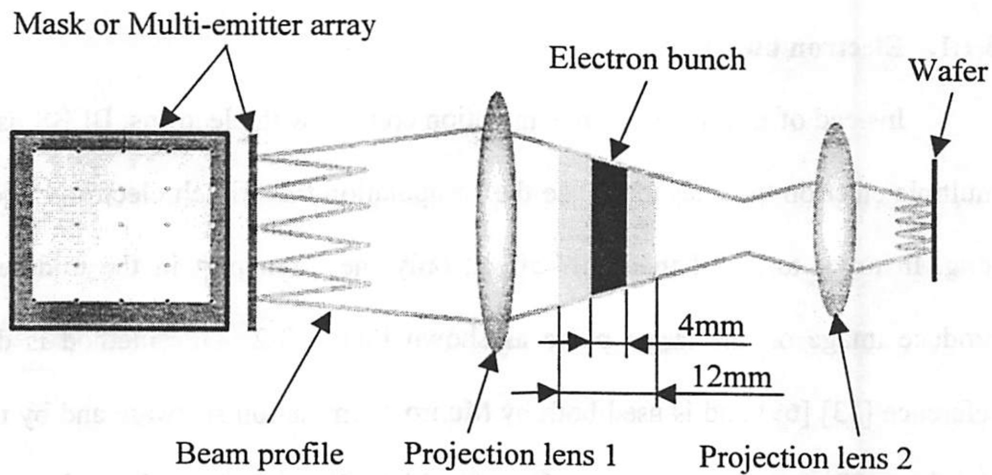

Figure 3-2. Schematic diagram of a typical simulated system with 25-emitter array. The 12mm long electron bunch is shown in the diagram.

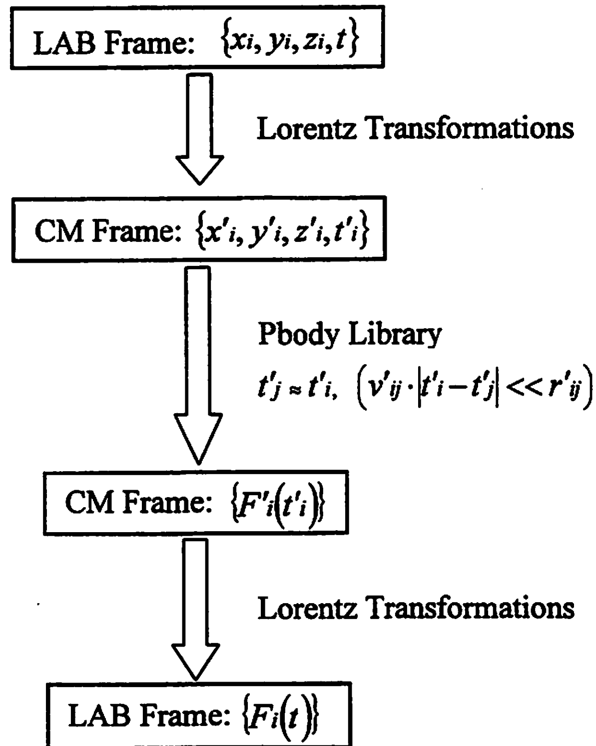

Figure 3-3. Flowchart of force calculations.

Equation 3-1 [70].

$$
\begin{aligned}
x'_i &= x_i \\
y'_i &= y_i \\
z'_i &= \gamma(z_i - v \cdot t) \\
t'_i &= \gamma(t - v \cdot z_i / c^2)
\end{aligned}
$$

where $\gamma = \dfrac{1}{\sqrt{1 - v^2/c^2}}$ and v is the center of mass velocity of the electron beam.

Notice that the positions of different electrons correspond at a slightly different instant in the CM frame. However, the relative positions of the electrons only take

negligible changes within these time differences, as indicated by Equation 3-2. Therefore, simultaneousness is a good approximation in calculating forces. The forces are transformed back to the LAB frame before Pbody is called.

Equation 3-2 [71].

$$
\begin{aligned}
F_{xi} &= F'_{xi} / \gamma \\
F_{yi} &= F'_{yi} / \gamma \\
F_{zi} &= F'_{zi}
\end{aligned}
$$

3.2. Time iteration

BEBS updates the positions of the electrons through a special iteration algorithm of its own. There are two distinguished features of BEB's time iteration algorithm. First, it uses the time steps adaptively to reduce the amount of computations needed. Second, BEBS uses continuously interpolated forces to calculate ending positions.

Figure 3-4 shows the flowchart of time iteration. BEBS uses a trial time step Δt based on the result of the last time step. This section only discusses movements along the x direction. The movements along y and z are treated in the same way. As an example, the solid curve in Figure 3-4 shows the real trajectory of an electron i from t to Δt. The force $F_{xi}(t)$ experienced by this electron varies with time. BEBS approximates $F_{xi}(t)$ with $\tilde{F}_{xi}(t)$, which would be experienced by this electron if there were no Coulomb forces and all the electrons in the column traveled along straight lines, as shown in Figure 3-4. $\tilde{F}_{xi}(t)$ is further approximated with parabolic function $\tilde{F}_{xi}(\tau) \approx A_{xi}(\tau-t)^2+B_{xi}(\tau-t)+C_{xi}$, where the coefficients A_{xi}, B_{xi} and C_{xi} are solutions from the relations given by Equation 3-3.

Equation 3-3.

$$C_{xi} = \tilde{F}_{xi}(t)$$

$$A_{xi}(\Delta t/2)^2 + B_{xi}(\Delta t/2) + C_{xi} = \tilde{F}_{xi}(t + \Delta t/2)$$

$$A_{xi}(\Delta t)^2 + B_{xi}(\Delta t) + C_{xi} = \tilde{F}_{xi}(t + \Delta t)$$

Therefore,

Equation 3-4. $$F_{xi}(\tau) \approx \tilde{F}_{xi}(\tau) \approx A_{xi}(\tau - t)^2 + B_{xi}(\tau - t) + C_{xi},\ t \le \tau \le t + \Delta t$$

The dashed curve in Figure 3-5 is the trajectory of electron *i* calculated with the above force. Its ending point is

Equation 3-5. $$x_i^*(t + \Delta t) \approx x_i(t + \Delta t).$$

The validity of the above approximations are based on the assumption that all the electron trajectories are "straight enough" within time Δt, in other words, $|\mathbf{r}_i(t+\Delta t) - \mathbf{r}_i(t+\Delta t)| <= threshold$ for every electron in the column. A larger value of *threshold* will speed up the simulation with lower accuracy. On the other hand, a smaller *threshold* tends to increase the accuracy at the expense of simulation time. The optimal *threshold* at each beam current is obtained by lowering the *threshold* value until the spot size stops changing. For instance, *threshold=1e-6* is an appropriate choice for 30μA beam current. It takes 200 to 400 times steps for an electron to travel through the column. In the last step of each iteration, BEBS performs the threshold check. If the result is negative for some electron, Δt will be halved to make the approximation more accurate. On the other hand, if it works for two consecutive iterations, Δt will be double to speed

up the simulation. The accuracy of the time iterations is checked with two relativistic electrons traveling through the beam column. The percentage error of the final transverse displacement of each electron is within 0.1%.

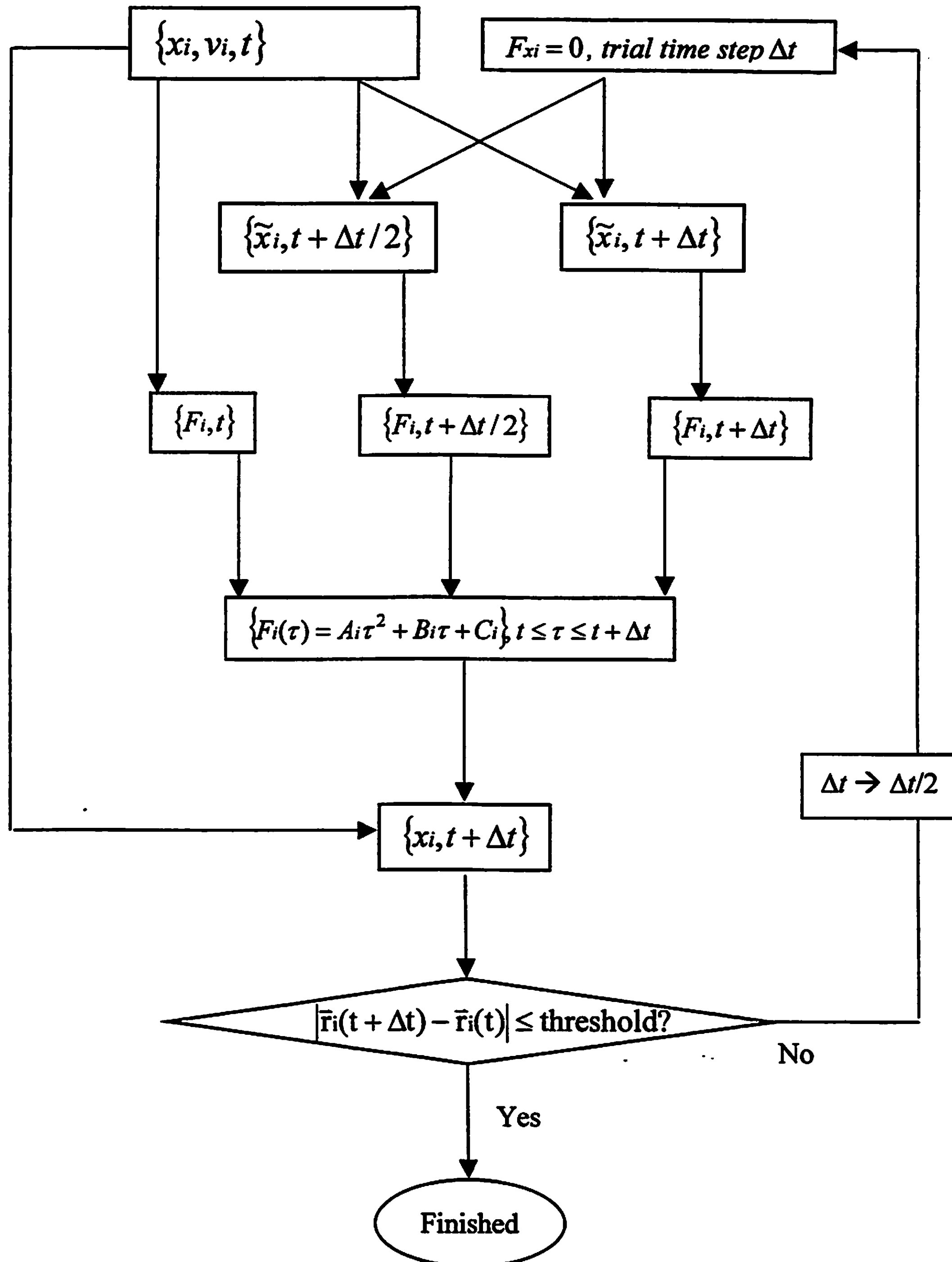

Figure 3-4. Flowchart of time iteration

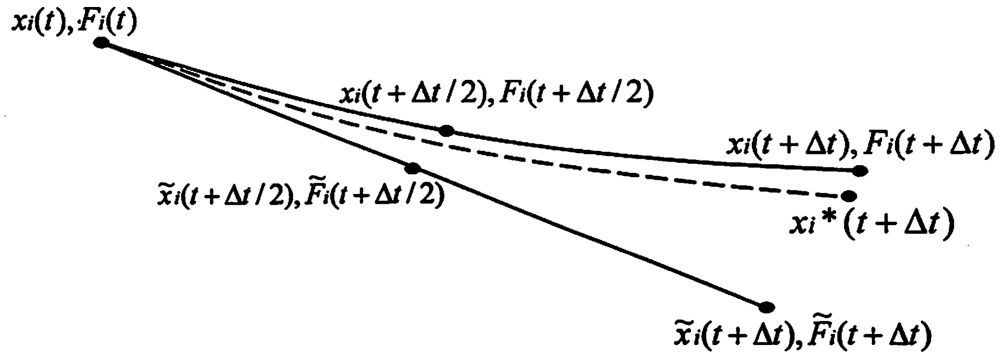

Figure 3-5. Schematic diagram of the "real trajectory" (solid curve), calculated trajectory (dashed curve), and "straight trajectory" of an arbitrary electron from time t to Δt. The forces used for iteration are measured on the "straight trajectory" at time t, $\Delta t/2$, and Δt.

3.3. Post-processing of data

As the electrons reach the target plane, BEBS stores their coordinates (x_i, y_i) and velocities (v_{xi}, v_{yi}). For a multi-emitter array system or beam projection system, the best image plane is defocused from the Gaussian image plane due to the space charge effect. In these systems, the major task of post-processing data includes measuring the size of the image blur and finding the best image plane.

Figure 3-6 illustrates the data processing algorithm with a 25-emitter array system. The algorithm starts with three trial target planes, where $z=z_1$, $z_1+\Delta z$, and $z_1-\Delta z$ respectively. A spot size R^z_i $(i=1,2,...25)$ is defined as the smallest radius of the circle that encompasses 50% of the electron image points of this spot as indicated in Figure 3-7. The center of the circle is the mass center of all the points. The sizes of different spots on

plane z vary due to the space charge effect, and the spot size of plane z is defined as $R(z) = max\{ R^z_i,\ i=1,2,...25\}$ based on the worse case consideration.

The values $R(z_1)$, $R(z_1+\Delta z)$, and $R(z_1-\Delta z)$ define a parabola $R(z)=a_1z^2+b_1z+c_1$ with minimum at $z_2=-\ b_1/2a_1$. Then the program starts with new trial planes at $z=z_2$, $z_2+\Delta z/2$ and $z_2-\Delta z/2$ respectively. The iteration continues until $\Delta z/2^n$<threshold. The z_n is the location of the best image plane, and $R(z_n)$ is the spot size (beam blur) of the system.

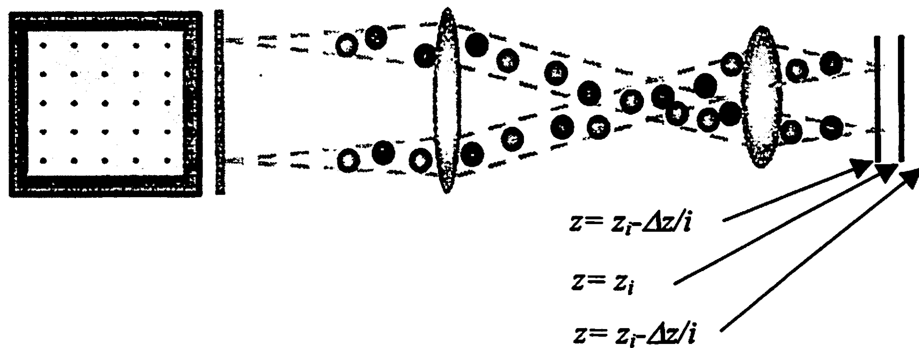

Figure 3-6. Spot sizes are measured at three different trail planes at $z=z_i$, $z_i+\Delta z/i$, and $z_i-\Delta z/i$ for each iteration. Only two beamlets are shown for clarity.

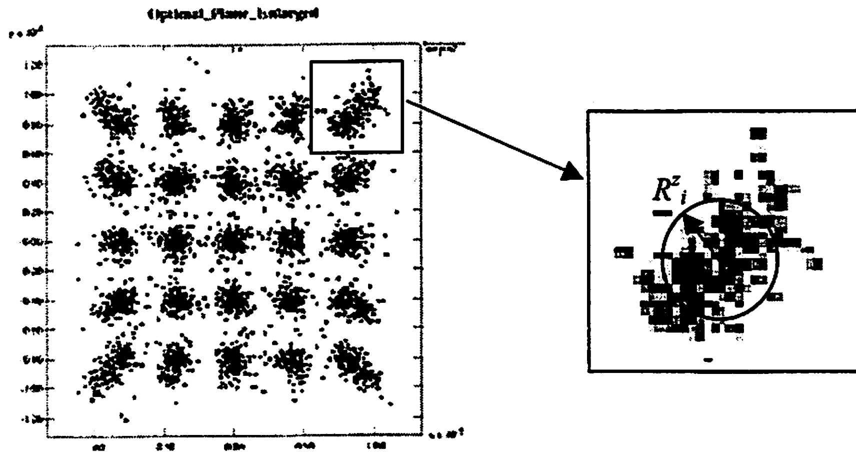

Figure 3-7. Measuring a beam spot *i* on a target plane *z*.

3.4. Special options in BEBS

A unique feature of BEBS is its special options for mechanisms studies compared with other electron beam simulators, including Munro's Software, which puts more emphasis on the engineering design. Every special option listed below leads to academic contributions presented in later chapters where the details of each option are also provided.

1. Identify the neighboring electrons of an arbitrary electron of concern and compute the forces caused by these electrons only. This special option gives the user the chance to study the relative influence of the neighboring electrons in creating image blur.

2. Directly generate stochastic beam blurs in simulation through the use of positrons. The space blurs are completely eliminated in this case. This option is the first of its kind among electron beam simulators and it gives users the capability to directly study the stochastic blurs in any beam configurations. The details of this option together with applications are covered on Chapter 5.

3. Separate the beam blurs caused by electron trajectory displacements and those caused by the electron velocity shifts through particle relocations. This option helps identify and compare the blurs of the two causes.

4. Switch on/off Coulomb interactions in different regions in the beam column. Although impossible to run in practice, these Gedanken experiments provide the chance to study the blur contributions from different regions in the beam column.

5. Introduce lens aberration in either of the projection lenses to study their effects. The choices of aberrations include astigmatism, axial astigmatism, coma, field curvature, distortion, and spherical aberration.

6. Introduce positive ions in the beam column to study their influence on the beam blur. Due to their large mass compared with electrons, the ions in the column are assumed to be stationary throughout the simulation.

3.5. Comparison with Munro's Software

In addition to the special options discussed in the previous section, a different force computation algorithm is the other major difference between BEBS and Munro's electron beam simulator. Instead of the FMM, Munro employs the Barnes-Hut (BH) method.

3.5.1. Barnes-Hut algorithm

The BH algorithm involves two steps [69]. In the first step, all the particles in the bunch are surrounded by a cubic box called the "root cell". This is subdivided into 8 smaller cells, until each particle has been assigned to a unique cell, as shown in Figure 3-8. In the second step, the inter-particle forces are computed. To compute the force upon particle *P* (see Figure 3-9), one starts from the root cell. Let L be its side length, and D the distance from the centroid C of the particles in the cell to particle P. In Munro's implementation of BH, if D>=L (as in Figure 3-9a), one computes the total force upon P by assuming that all the charge in the cell is located at the centroid C. On the other hand, if D<L (as in Figure 3-9b), then the cell is resolved into eight sub-cells and the procedure is repeated recursively. To obtain the force upon each particle, the above procedure is repeated for each point P where the particle is located. We will refer to this version of BH as the Munro type implementation.

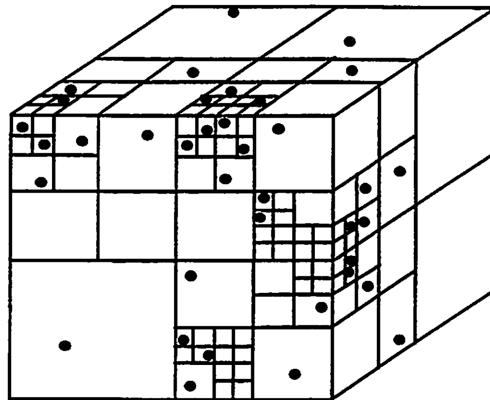

Figure 3-8. Organizing the particles in a tree structure.

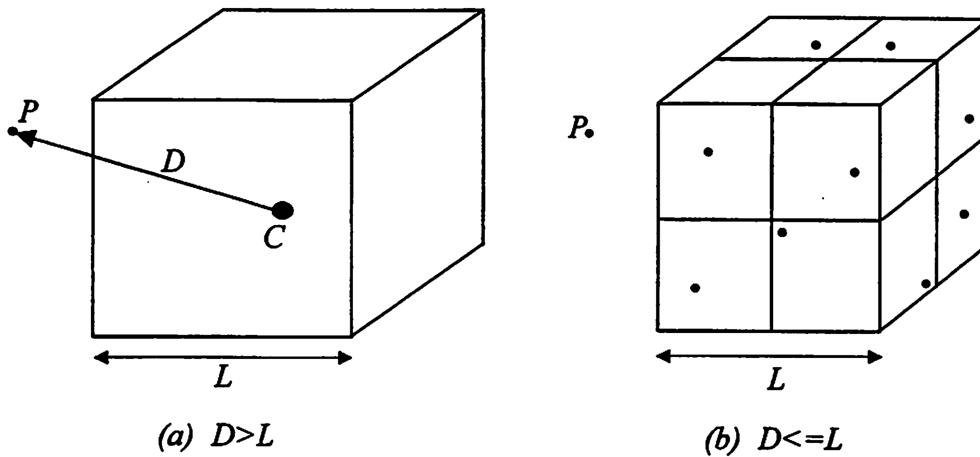

Figure 3-9. Force calculations in Barnes-Hut Method.

3.5.2. Accuracy and speed comparison

We compare the accuracy of the transverse forces computed with the Munro type implementation for BH and the transverse forces computed with FMM for the electron

bunch given in Figure 3-10. The electron bunch has the same geometry as the electron bunch passing the crossover region in Figure 3-1 if the beam convergence angle is 1.5mR.

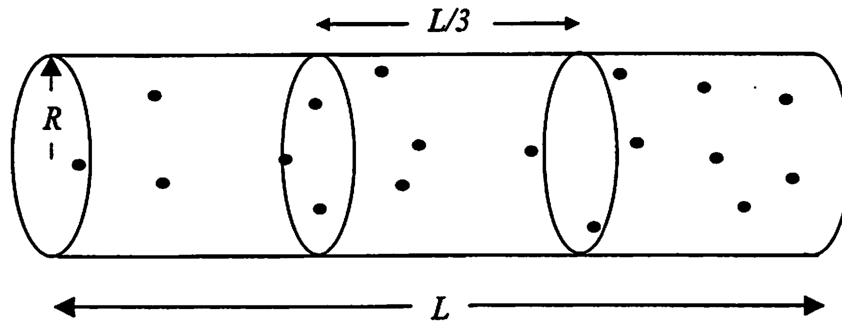

Figure 3-10. The electron bunch used in the accuracy comparison between Barnes-Hut and FMM. $R=240\mu m$ and $L=12mm$.

The simulation computes the transverse forces F_x and F_y on an arbitrary electron located in the 4mm part in the middle of the electron bunch with (a) FMM, (b) BH, and (c) direct calculation of forces from every other electron in the bunch. The forces computed with FMM and BH are compared with forces calculated directly and the percentage errors for FMM and BH are presented in Figure 3-11.

The simulation shows that the transverse forces computed with BH on average have 9% errors compared the forces predicted by direct calculations at 5μA beam current. The percentage error tends to decrease as the beam current increases. The error for the forces calculated with FMM, on the other hand, is always within 0.1% for 5μA to 30μA.

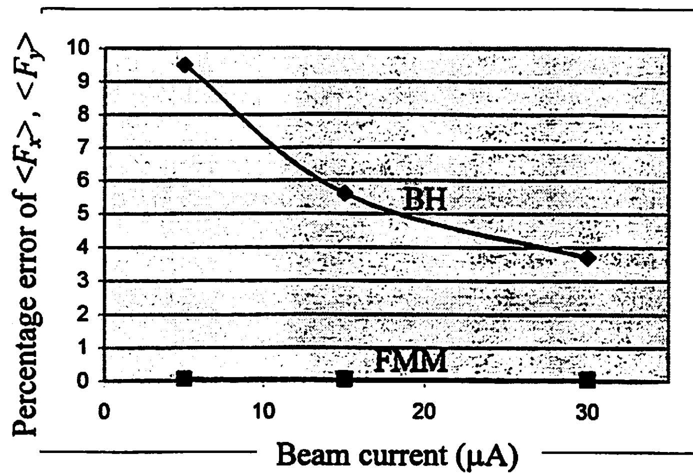

Figure 3-11. Percentage errors for the transverse forces computed with BH and for the forces computed with FMM. The percentage errors corresponding to FMM are below 0.1% in the graph.

Figure 3-11 shows that the percentage errors decrease with beam current. The following argument provides a qualitative explanation to this phenomenon. Figure 3-12 (a) and (b) are two electron bunches of the same geometry with electron densities $n_a < n_b$. P_a is an arbitrary point in configuration (a) and P_b is the corresponding point in (b). Let F_a and F_b be the total transverse forces measured respectively at these two points. In order to compare the percentage errors of these forces calculated with BH, electron bunch (b) is scaled to (c) such that $n_a = n_c$. Now, the shaded region in (c) has the same geometry and same electron number density as electron bunch (a). Thus, the force F_{shaded} caused by the electrons in the shaded region has the same percentage error as F_a. On the other hand, the unshaded region has larger cells with more electrons compared to the shaded region as these cells are relatively further away from P_c. Thus, the statistical fluctuation and

percentage error of $F_{unshaded}$ calculated with BH is smaller than that of F_{shaded}. Therefore, The total transverse force $F_c = F_{shaded} + F_{unshaded}$ has less percentage errors than F_a. In other words, the percentage errors of forces decrease at higher current density.

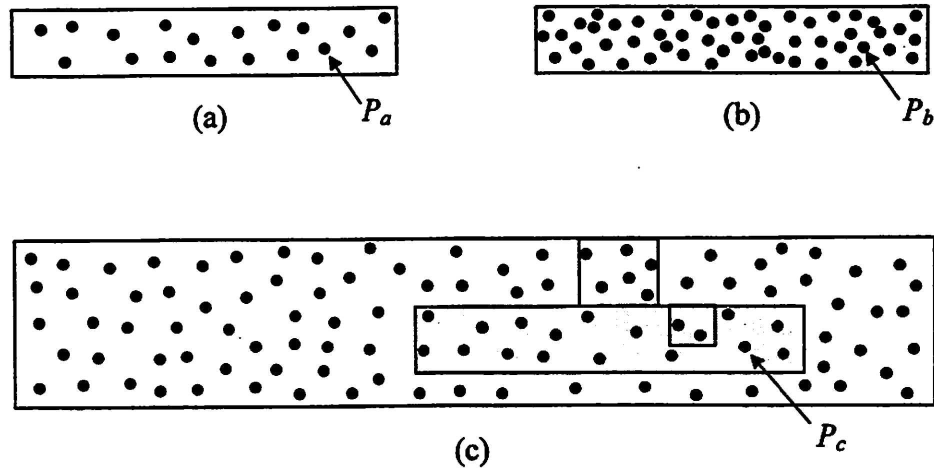

Figure 3-12. Electron bunch (a) and bunch (b) with electron densities $n_a < n_b$ and the scaled electron bunch (c) with $n_c = n_a$.

Errors in the force calculations certainly influence the accuracies of the final beam blur. The following back-of-the-envelope calculation provides a rough estimate of the percentage error for the corresponding beam blurs based on physical intuition. The accuracy of the estimates requires more rigorous studies.

Results given in the next chapter show that 90% of the beam blur is caused by the transverse forces in the region within 200mm of the crossover at 5μA beam current. The

averaged beam radius of this region $R=315\mu m$ is used to estimate the percentage error in force calculations with BH. The corresponding electron number density is the same as that of a 240μm radius electron bunch at 8.7μA. Thus, the calculated forces in the these two beam configurations also have the same percentage errors, which are more than 7% for the BH method, as indicated in Figure 3-11. In other words, the transverse forces calculated with BH in the crossover region are on average has 7% errors compared with the exact forces.

Simple argument shows that $F \propto \frac{1}{d^2} \propto I^{\frac{2}{3}}$, where F is the total force upon an arbitrary electron in an electron bunch, and d is the average spacing of the electrons. Results given in Chapter 7 state that the stochastic blur $B_{st} \propto I^{0.62}$, and the space charge blur $B_{sp} \propto I$. So, $B_{st} \propto F$, and $B_{sp} \propto F^{\frac{3}{2}}$. Therefore, the final beam blur will be roughly 7% smaller if the errors for the forces do not average out between iterations. For 30μA beam current, the estimated error for the beam blur will be around 3% instead of 7%. Similarly, the estimated error for the beam blur computed with FMM is within 0.1% for currents between 5μA and 30μA.

There are two likely reasons for the higher accuracy achieved the by FMM in the above example. First, FMM uses direct calculations for the electron interactions between neighboring cells, which is not present in the Munro type implementation of BH. This is especially important when the neighboring electrons make significant contribution to the

total transverse force. Secondly, FMM includes up to the 5th term in the spherical harmonic expansion while the BH implemented above only uses the monopole term.

The high accuracy of FMM is achieved at the cost of speed and runtime. Figure 3-13 compares the run time per iteration N particles. The runtime test for BH was carried out by the Munro type implementation with 400MHz processors [69] while the runtime for FMM was measured with BEBS running on ten 500MHz processors. As the graph shows, simulation with BEBS is around 5 times slower compared with Munro's simulator. Here, the run time for BH and FMM are corresponding to different accuracies. The FMM is implemented only for high accuracy force calculations. Thus only run time at high accuracy are available.

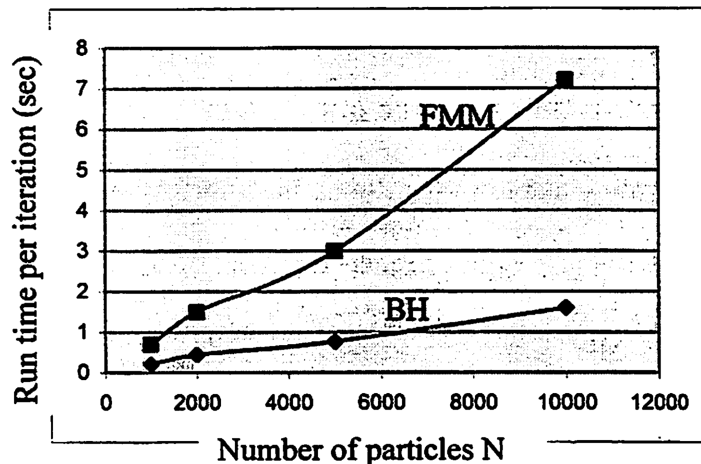

Figure 3-13. Comparison of run time per iteration between FMM and BH with N particles.

4 Beam Blur Contributions in Multi-emitter Array Systems

4.0. Introduction

This chapter first presents how beam blur contributions vary along the optical axis in Section 4.1. Next it will discuss how the electrons from the same beamlet and electrons from different beamlets interact and produce beam blur in Section 4.2. The summation rule of the blur contributions will also be presented in this section. The topics covered in this chapter were first investigated by the author and Neureuther [25].

4.1. Blur contribution along the optical axis

Studying how Coulomb interactions in different regions contribute to the final spot size helps identify the regions producing most of the beam blur. This will provide insight to new strategies for beam-blur reduction. Figure 4-1 shows the schematic diagram for the simulated 4X demagnification system. The emitter array consists of twenty-five emitters with 200μm spacing. The illumination convergence angle of each beamlet is Gaussian distributed with standard deviation equal to α. The whole column is divided into eleven labeled regions.

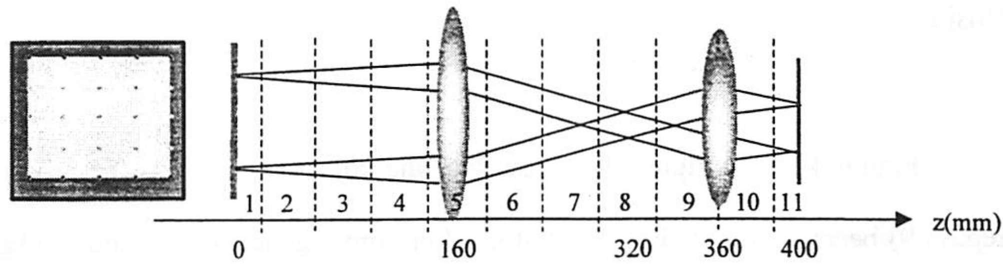

Figure 4-1. Schematic diagram of the simulated system measuring beam blur contribution along the optical axis. V=100kV, δV=15V for all the simulations.

The crossover is around z=320mm in region 9. With one of the BEBS' special options, Coulomb interactions are turned on only in one region for a single run, and the final spot size is measured on the best image plane. The results are presented in Table 4-1 and Figure 4-2. Here, the z value corresponds to the center of each region. Total beam blur d_0 is measured when the forces are on throughout the column, and value a is the linear summation of the blurs from all eleven regions.

d_0/a gives the degree of coherency between different regions. A coherency close to one implies that the blurs from different regions are combined in an almost linear fashion, while a relatively small coherency indicates more randomness and more frequent change of force directions as electrons travel in the column.

The data in Table 4-1 shows coherency increases with beam currents and decreases with illumination convergence angle. This agrees with the microscopic

interpretation that the stochastic forces make more directional changes at higher electron densities.

Figure 4-2 and Figure 4-3 show that the contribution from the crossover region (region 9) becomes more significant at smaller convergence angles and at higher current beam currents. Numerically, this contribution is roughly proportional to I/α. On the other hand, the regions near the mask and the wafer contribute little, in spite of the high electron densities.

blur contribution (*nm/40mm*)			α(mR)	0.5	1.5	2.5	1.5
region #	*z* (*mm*)	region length (*mm*)	I(μA)	5	5	5	10
1	10	20		0	0	0	0
2	40	40		1	0	0	1.7
3	80	40		1.7	1	0	1.9
4	120	40		2.3	1.7	1.6	2.5
5	160	40		1.9	1.8	1.7	3.4
6	200	40		3.3	3	2.7	5.2
7	240	40		4.1	4	3.2	7
8	280	40		8.9	7	4.9	13.3
9	320	40		34	10.5	7.1	23
10	360	40		9.8	6	4.4	13.5
a(nm)				69	36.6	27	74.9
d_0(nm)				51	34	25	53
coherency				0.74	0.93	0.93	0.71

Table 4-1. Blur contribution from different regions along the optical axis. The contribution from the region near the mask or the wafer is normalized to a 40mm region length for comparison.

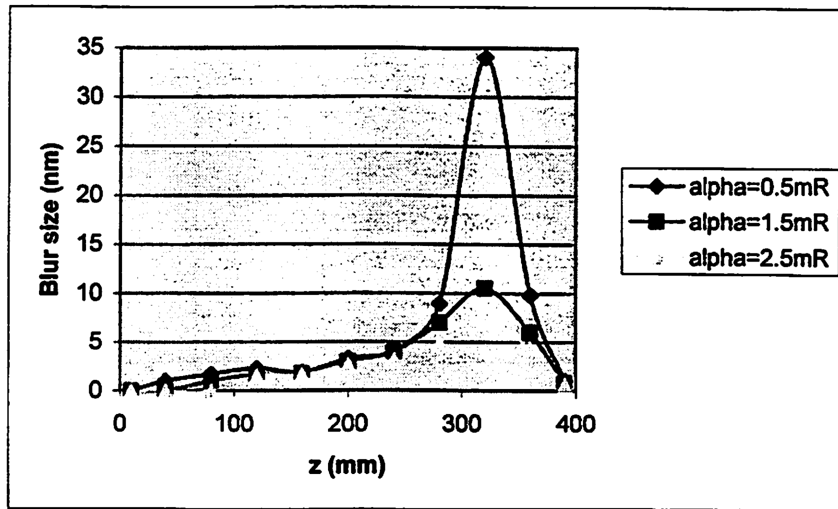

Figure 4-2. Beam blur contribution along the optical axis at different convergence angles. Here $I = 5\mu A$.

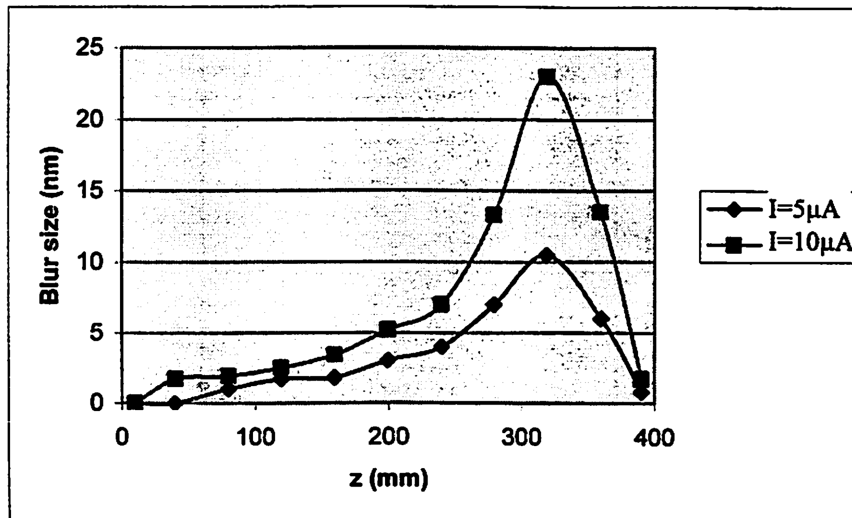

Figure 4-3. Beam blur contribution along the optical axis at different beam currents. Here beam convergence angle $\alpha=1.5mR$.

4.2. Inter-beamlet, intra-beamlet electron interactions and the summation rule

4.2.0. Mask configurations

The electron beam in the column consists of multiple beamlets. To Understand how these beamlets interact and contribute to the final beam blur is crucial to the mask design. Only the central beamlet is measured on the wafer for the simulations in this section, while other beamlets are turned on and off to study the effects.

Figure 4-4 shows the mask or emitter configurations for different test cases. Table 4-2 summarizes the corresponding blur size of the central beamlet for each of the mask configurations. One notices that the two 3-beamlet configurations of produce almost the same spot size.

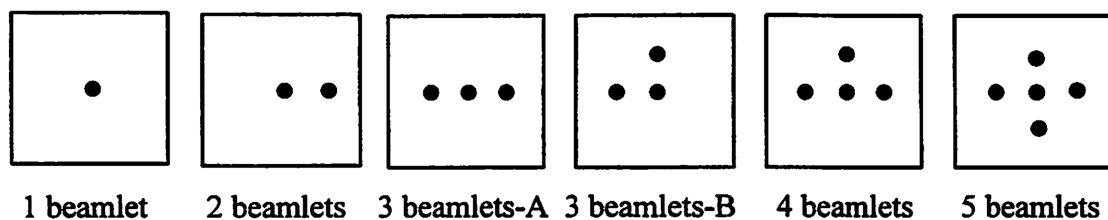

Figure 4-4. Different configurations of the 25-emitter array. All the unmarked emitters are turned off. The spacing between emitters is 200μm.

alpha(mR)	beamlets	1	2	3-A	3-B	4	5	
0.5		26	46	60	61	69	78	
1.5		10	22	30	30	35	40	spot size D (nm)
2.5		5	15	20	22	25.5	28	
0.5		676	2116	3600		4761	6084	
1.5		100	484	900		1225	1600	spot area $D^2(nm^2)$
2.5		25	225	400		650.3	784	

Table 4-2. Blur size of the central beamlet for each of the mask configurations in Figure 4-4. The current of each beamlet is *0.8μA*, which corresponds to *20μA* for 25 beamlets.

4.2.1. Summation rule for beam blur contributions

Figure 4-5 shows the area of each spot against the number of beamlets that on. The linear behavior of each data set clearly indicates that the blur contributions are combined in a root mean square basis, namely:

Equation 4-1.
$$D^2 = {d_0}^2 + \sum_{i=1}^{N} {d_i}^2$$

where D is the central beam blur, d_0 is the blur contribution from the electron-electron interaction within the central beamlet itself, and d_i is the blur contribution from the ith neighbor beamlet. Owing to symmetry, the d_i's at the same convergence angle are equal. Thus:

Equation 4-2. $$D^2 = d_0^{\,2} + N \cdot d^2$$

for each convergence angle α. The values of d^2 can be obtained as the slopes of the corresponding linear plots in Figure 4-5. The values of d are summarized in Table 4-3.

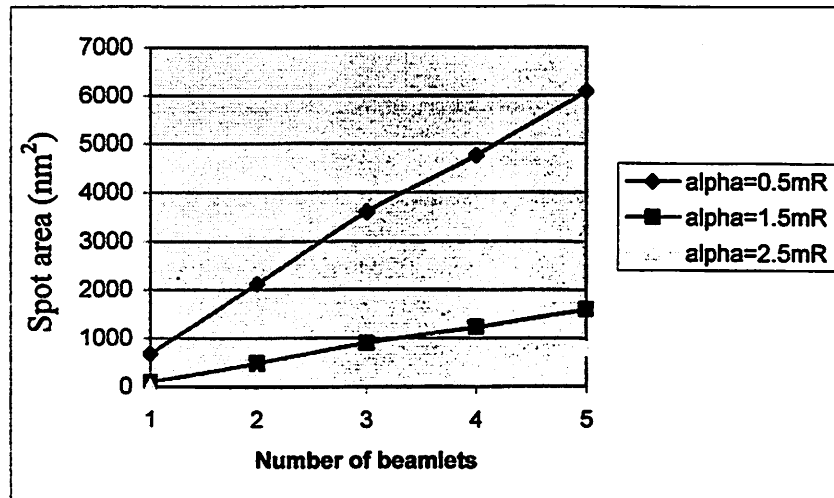

Figure 4-5. Spot area of the central beamlet versus the total number of beamlets that are switched on. Configuration A was used in the simulation for the 3-beamlet case.

4.2.2. Inter-beamlet and intra-beamlet blur contributions

Figure 4-6 and Figure 4-7 draw comparisons between d_0 and d. As can be seen, a neighbor beamlet heavily contributes to the central beam blur at large convergence angles and at high beam currents. At smaller angles, however, the effect of a neighbor beamlet prior to the crossover tends to cancel with its effects beyond the crossover. This phenomenon will be discussed in Chapter 5.

	I=0.8 (μA/beamlet)				alpha=1.5 (mR)	
alpha (mR)	d_0 (nm)	d (nm)		I (μA/beamlet)	d_0 (nm)	d (nm)
0.5	26	38		0.8	10	19.6
1.5	10	19.6		1.2	12.5	31.6
2.5	5	14		1.6	16.5	43.8

Table 4-3. Beam blur contribution d from a neighbor beamlet and the blur contribution d_0 from the central beamlet itself. d is obtained from Equation 4-2.

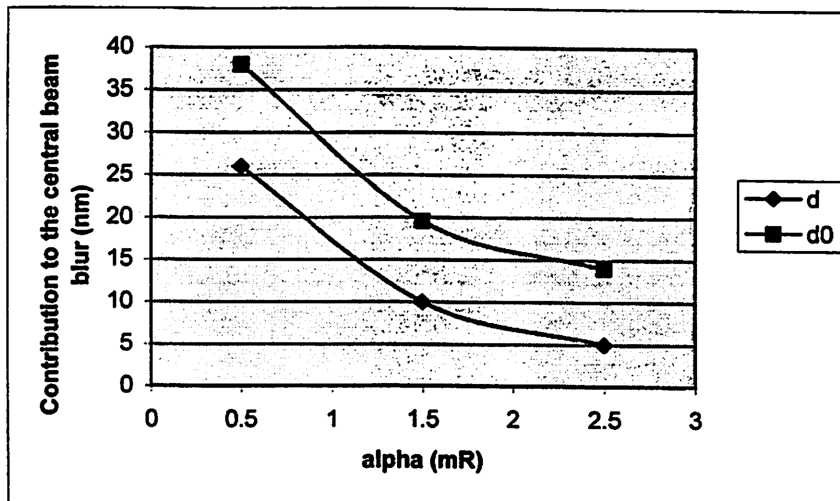

Figure 4-6. Comparison between intra-beamlet contribution d_0 and the inter-beamlet contribution d at different convergence angles.

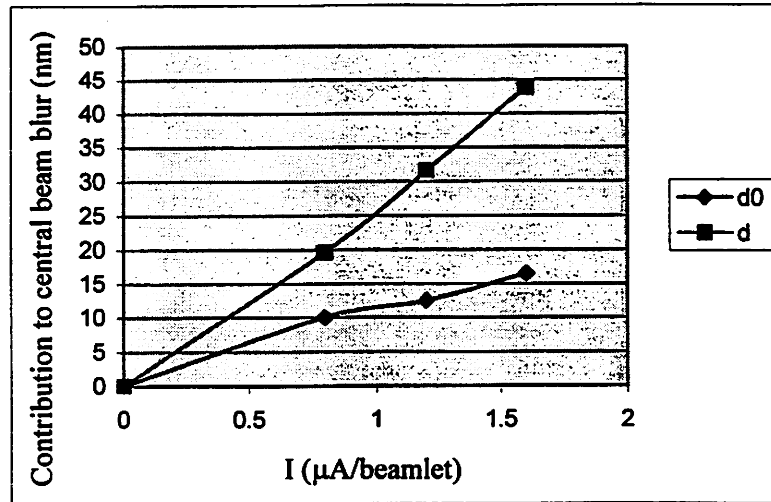

Figure 4-7. Comparison between intra-beamlet contribution d_0 and the inter-beamlet contribution d at different beam currents.

4.2.3. Inter-beamlet blur contribution and emitter spacing on the mask

In all the previous test cases, the spacing between emitters on the mask is fixed at 200μm. In this section, the relationship is investigated between d and the initial separation of the corresponding emitters on the mask. Similar to Section 4.2.1, d is obtained from Equation 4-2, and D_2 and d_0 are measured in simulations. The results are summarized in Table 4-4, Figure 4-8 A and B. As can be seen, the blur contribution from a neighbor beamlet decreases much more slowly than the inverse square law for Coulomb interactions.

I=0.8μA/beamlet, α=1.5mR

Distance (grid)	0.5	1	2	3	4	5	6	7
D2 (nm)	24	22	21.5	21	20	18.5	17	16
d0 (nm)	10	10	10	10	10	10	10	10
d (nm)	21.8	19.6	19	18.5	17.3	15.6	13.7	12.5

I=0.8μA/beamlet, α=2.5mR

Distance (grid)	0.5	1	2	3	4	5	6	7
D2 (nm)	16	15	14	13.5	13	12	11.5	11
d0 (nm)	4	5	5	5	5	5	5	5
d (nm)	15	14	13	12.5	12	11	10.4	9.8

I=1.2μA/beamlet, α=1.5mR

Distance (grid)	0.5	1	2	3	4	5	6	7
D2 (nm)	37.5	34	30	27.5	26	25	24	23
d0 (nm)	12.5	12.5	12.5	12.5	12.5	12.5	12.5	12.5
d (nm)	35.4	35.4	27.3	24.5	22.8	21.7	20.5	19.3

Table 4-4. Beam blur contribution *d* caused by inter-beamlet electron interactions varies with the distance between the emitters on the mask. A grid here equals 200μm.

(A) I=0.8μA/beamlet

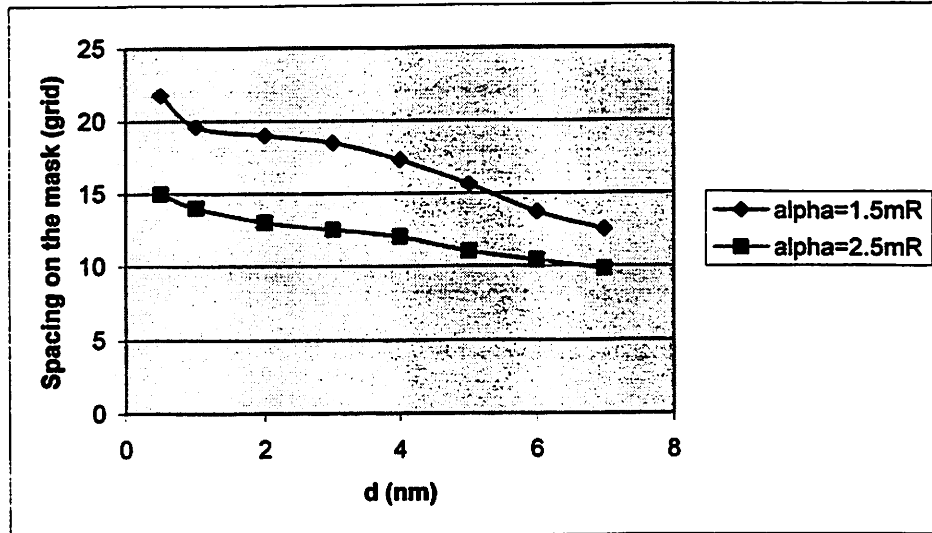

(B) α=1.5mR

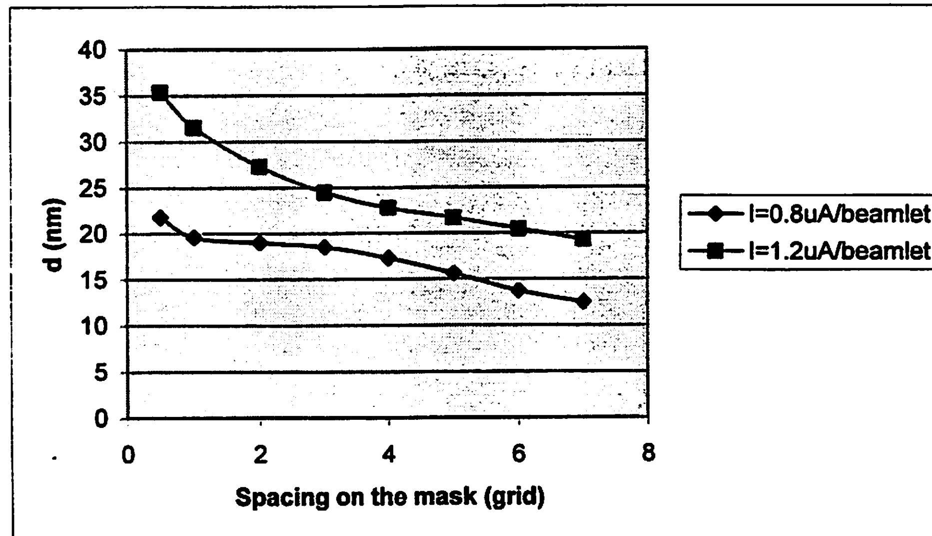

Figure 4-8. Beam blur contribution *d* from a neighbor beamlet decreases with the corresponding emitter spacing on the mask. One grid equals 200μm separation on the mask.

4.3. Conclusions

Studies show that beam blur is mostly produced in the crossover region in a multi-emitter array system, which implies that blur reduction techniques should focus on interactions in this region. Meanwhile, the blur contributions caused by inter-beamlet electron interactions dominate over those caused by intra-beamlet electron interactions, especially at large convergence angles. Further study is needed in order to find efficient ways to isolate and manipulate inter-beamlet interactions in an experimental setup. Simulation results demonstrate that the beam blur contributions from different beamlets can be combined on a root mean square basis.

5 Stochastic Coulomb Interactions and Neighboring Electrons

5.0. Introduction

Mkrtchyan's Nearest-Neighbor Theory [6] is one of the analytical models used to study stochastic interactions in e-beam lithography. This chapter provides the methodology to verify one of Mkrtchyan's basic assumptions, namely that the stochastic force upon each electron in a beam column is dominated by the contribution from the nearest neighbor electron. Section 5.1 introduces the basic setup of the test system. Section 5.2 discusses the number of neighboring electrons in different regions along the optical axis. Section 5.3 addresses the issue of how the number of neighboring electrons affects the transverse stochastic forces. The reader may refer to Chapter 2 for a brief introduction to the analytical models on the electron stochastic effects.

5.1. System setup

A basic test geometry of a crossover in a lens free region equidistant between two lenses was used to explore the nature of the electron-electron interactions. The test beam geometry is shown in Figure 5-1. The crossover is midway (at 100mm) in the 200mm lens free analysis domain. The electron emitter for this study was idealized to inject

electrons with all the same energy ($\delta E = 0$) and the angle was computed from the random lateral position so that each electron if undeflected by others would pass through the mathematical crossover ($\delta\alpha = 0$). An ideal lens was assumed to follow the simulation domain, which focused the crossover to a point on an image plane 100mm beyond the simulation domain. This lens, whose focal length is independent of electron energy, provides a means of directly observing beam blur due to electron-electron Coulomb interactions. For the studies shown below, the beam energy was 100kV and the radius of the initial beam was 1mm. The simulation domain was a 200mm cylindrical tube with a 1mm radius.

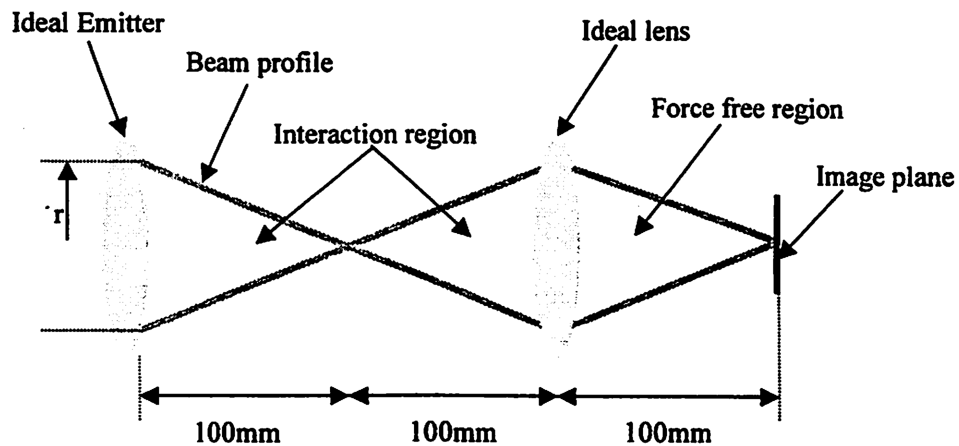

Figure 5-1. Test beam geometry. The system parameters are: $V=100kV$, $\Delta E=0$, $r= 1mm$, $f_{emitter}=100mm$, $f_{lens}=50mm$.

5.2. Number of neighboring electrons

Simulation was carried out at beam currents of 1, 10, and 20μA, respectively. The simulation was initialized by first running the column at the current for about two ns to completely fill the simulation domain. At a later time step, those electrons with instantaneous forces exceeding threshold value F_{cutoff} were singled out for the subsequent analysis. The positions and forces of these electrons give insight to the locations and the sizes of strongly interacting electron clusters, which make a major contribution to the beam spot size. A threshold of 10^{-20} N was chosen for 1μA and 10^{-19} N for 10 and 20μA. Forces below this threshold were insignificant with respect to influencing beam spot size, as confirmed by separate tests. For each electron, all its neighboring electrons are identified and located. This allows the size of electron clusters to be seen as a function of position along the beam. It also allows the contributions to the transverse force to be analyzed as a function of the number of neighbors included in the calculation.

The number density of electrons with N neighbors is plotted as the function of positions along the optical axis at $1\mu A$ in Figure 5-2. At $1\mu A$ about *7600* electrons are in the simulation domain at any instant. Of these, about *2700* (or *35%*) experience forces greater than $10^{-20}N$ as indicated by the data labeled total. The curve labeled $N=1$ corresponding to the electrons with only one nearest neighbor. These electrons account for most of the strong interactions more than *20mm* away from the crossover and about 37% of the strong interactions overall. Near the crossover the N>=3 and N<=8 curve corresponding to those electrons with three to eight neighbors rises, and right at the crossover many of the electrons experiencing strong forces have 9 or more neighbors.

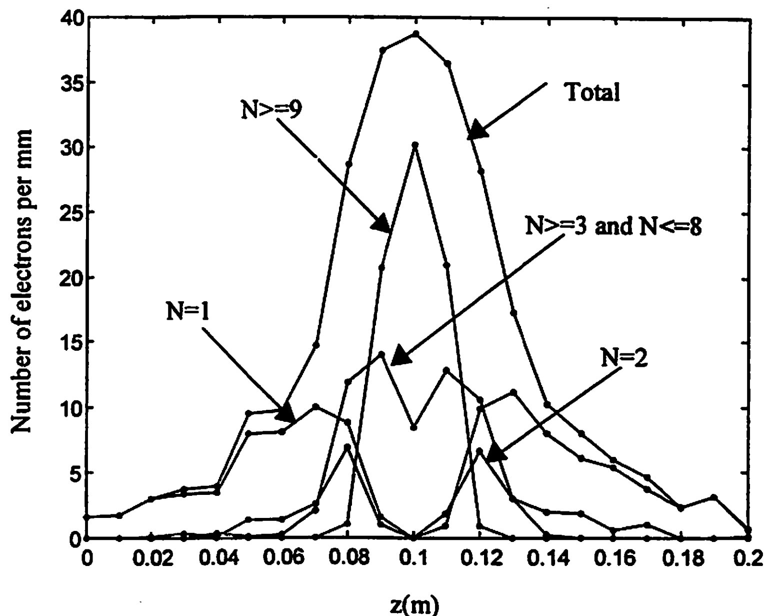

Figure 5-2.Number of neighbors electrons vs. axial position for I=1 μA and $F_{cutoff}=10^{-20}$ N.

Figures 5-3 and 5-4 show the number density of electrons with N neighbors along the column for beam current increasing to *10* and *20μA*. The curves are quite similar in shape to that for 1 μA. However, note that the vertical axis has been scaled proportional to beam current. The area is about 9,062 electrons or *12%* of the 76,000 electrons in a *10μA* beam. The decrease in the cases with less than 9 neighbors at the crossover is quite noticeable. As might be expected, the shape of these curves generally follows the number of electrons expected to be within a sphere with a radius of 48 um. Fortunately, this also indicates that the observed trends are likely scaleable to slightly lower force thresholds at which as much as 30% of the electrons undergo transverse-displacements and produce beam blur.

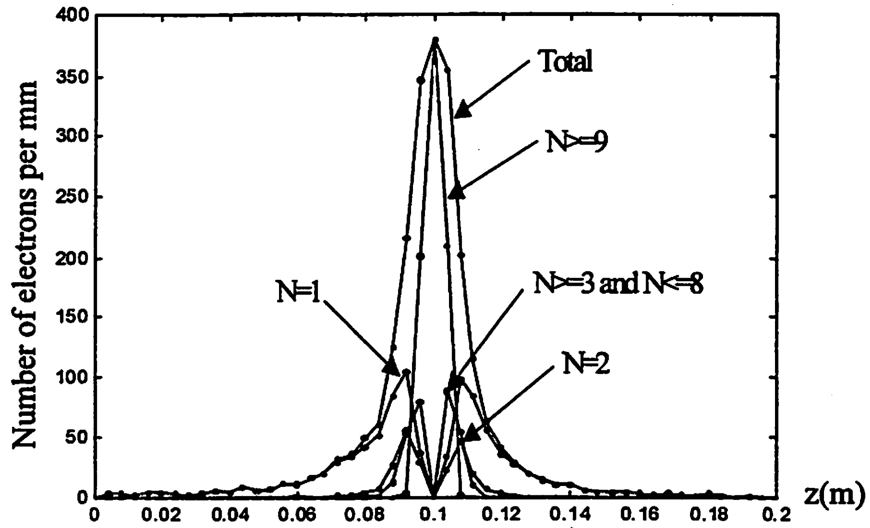

Figure 5-3. Number of electrons with N neighbors vs. axial position for I=10μA and $F_{cutoff}=10^{-19}N$.

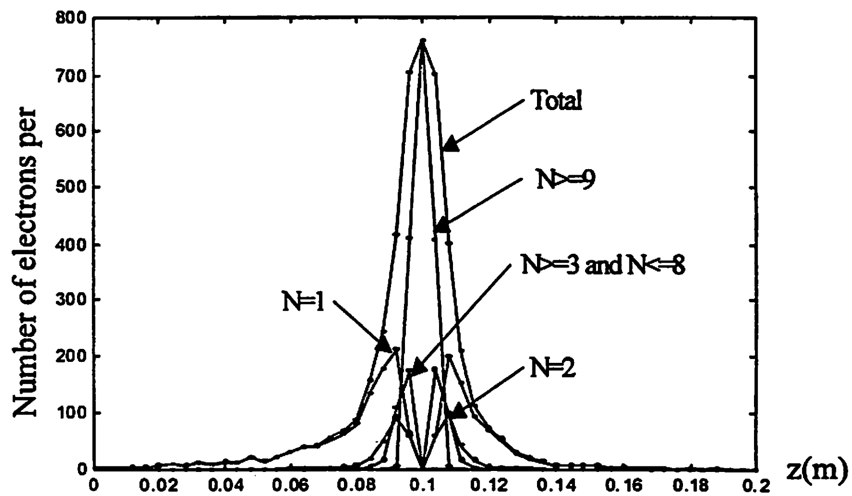

Figure 5-4. Number of electrons with N neighbors vs. axial position for I=20μA and $F_{cutoff}=10^{-19}N$.

5.3. Effect of neighboring electrons upon transverse forces

The contribution to the transverse statistical force from various numbers of neighbors at a 1μA beam current is shown in Figure 5.5. The vertical axis shows the force ratio for systematically including more neighbors. The horizontal axis shows the net transverse force on a logarithmic scale. The lowest data set is the ratio of the magnitude of the transverse force for two nearest neighbors compared to the ratio for one. The result is then shifted downward by one. Hence, any deviation from zero greater than 0.1 (49% of the electrons) indicates that a second neighbor affects the force by more than 10%. It is notable that at forces even above $10^{-18}N$ more than one nearest neighbor is participating.

Similar data sets are shown for 3 neighbors vs. 2 neighbors, 6 vs. 3, 10 vs. 6, and the total vs. 10. Again, a deviation from 5, 10, 15, and 20 by more than 0.1 indicates that the force changes by more than 10% when the additional neighbors are introduced. The corresponding percentage of the electrons is also given in the graph. The curves become quite compact in moving up to more nearest neighbors, especially for forces above 10^{-18}. One exception is the large blur for the total versus the 10-neighbor curve, and this is attributed to the presence of a more macroscopic space charge effect. As more and more neighbors are included, the force evaluated becomes closer and closer to the real statistical force, and the force ratio converges to one. For current of $1\mu A$, F_{10xy} is a good approximation to the real transverse statistical force as seen on the graph. In this case, 52% of the forces are more than 10% off (83% are larger and 17% are smaller) if one adopts the nearest neighbor approximation.

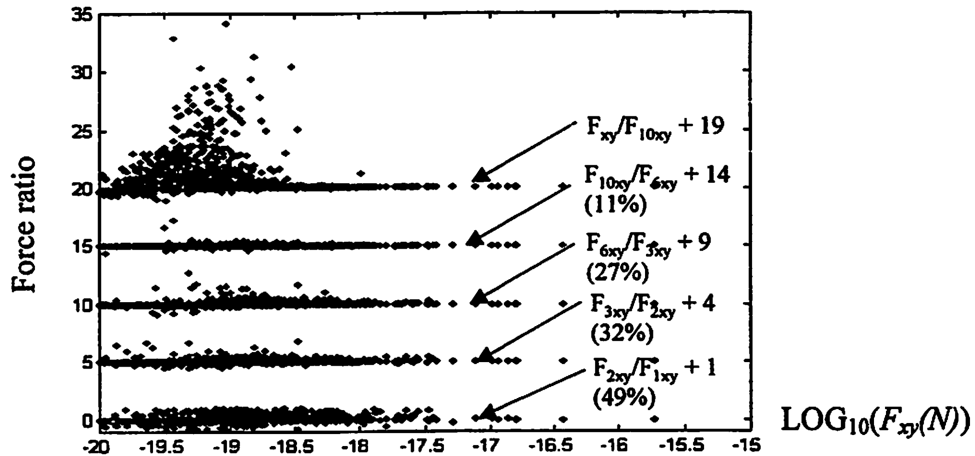

Figure 5-5. Effect of neighboring electrons upon transverse forces for I=1 μA and $F_{cutoff}=10^{-20}$ N.

Figures 5-6 and Figure 5-7 show the contribution to the transverse statistical force from various numbers of neighbors at 10 to 20 μA. An order of magnitude increase in beam current causes a two order of magnitude translation of the data set to higher forces. This is because the tenfold increase in beam current causes a tenfold decrease in the average spacing, which results in a two order of magnitude increase in the typical force. The spread in the data beyond a deviation of 0.1 is now much greater, and the increased spread becomes particularly noticeable even when 6 and 10 neighbors are added. At *10μA* it is likely the norm rather than the exception to have several nearest neighbors contributing to the force when passing through the crossover. Since multiple neighbors become important about *10mm* prior to the ideal crossover where the *10μA* current corresponds to a current density of $30mA/cm^2$, this current density might serve as a rule of thumb for when multiple neighbor contributions are completely dominating.

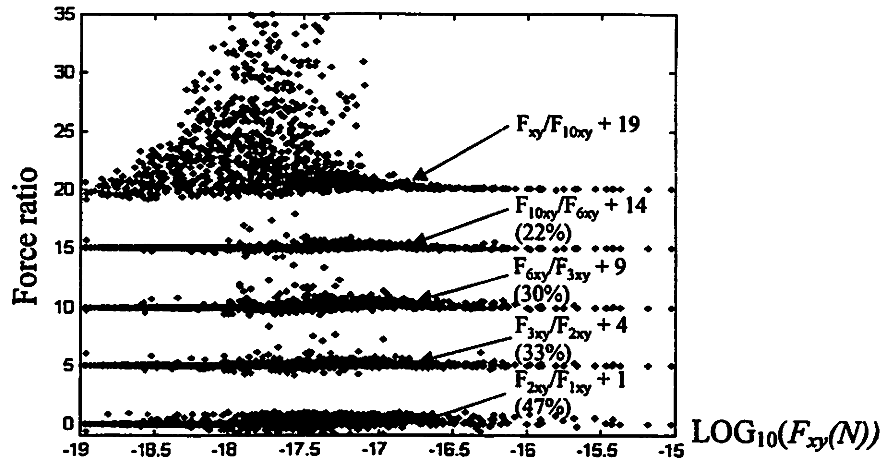

Figure 5-6. Effect of neighboring electrons upon transverse forces for I=10μA and $F_{cutoff}=10^{-19}$ N.

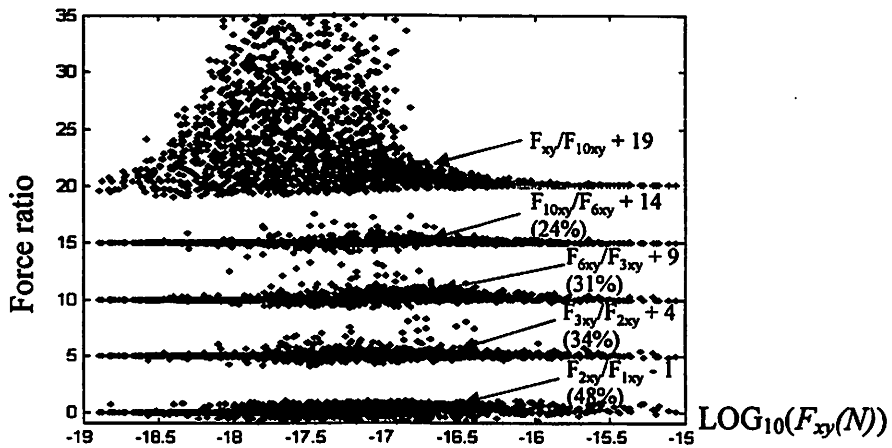

Figure 5-7. Effect of neighboring electrons upon transverse forces for I=20μA and $F_{cutoff}=10^{-19}$ N.

5.4. Conclusions

Analysis of a basic crossover showed that strong transverse-deflection forces were associated with high particle density. More importantly, interactions with multiple rather than nearest neighbors almost immediately became the norm rather than the exception. In practical systems where crossovers are not ideal, the current density might be used as a guide, with strong multiple neighbor interactions being observed at $10mA/cm^2$ and clearly dominant at $30mA/cm^2$. The corresponding typical electron inter-particle spacings are $62\mu m$ and $43\mu m$, respectively.

6 Structure of Stochastic Coulomb Interactions

6.0. Introduction

Traditionally, the stochastic beam blurs have been considered as random and uncorrectable, until a puzzling result was discovered. Jansen [26] predicted that the homocentric beam with a crossover and the homocentric parallel beam in Figure 6-1 produce the same spot size in spite of the high electron densities in the crossover regions. The prediction was later confirmed in simulations [41] [42]. To explain this puzzling result, Jansen suggested that some cancellation mechanism in stochastic interactions reduces the final beam blur in the configuration with a crossover. Nevertheless, the sophisticated mathematical formulation of his model failed to give convincing physical insight into this problem.

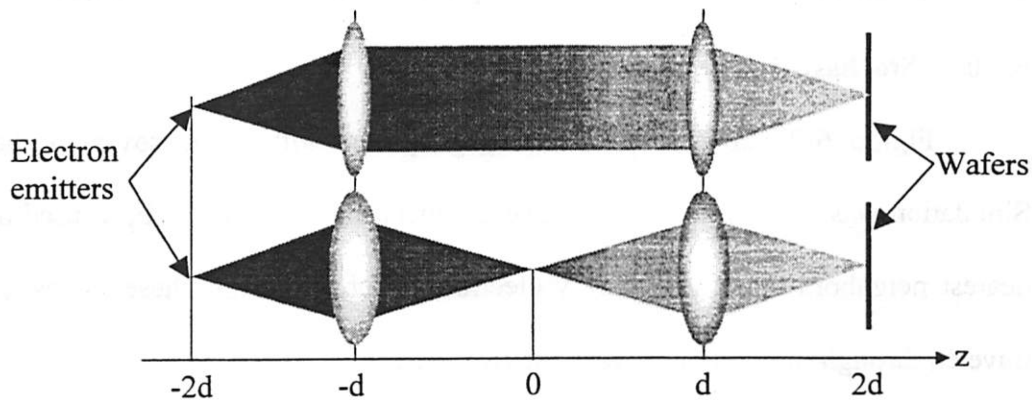

Figure 6-1. The homocentric beam with a crossover, and the homocentric parallel beam that produces the same spot size, as predicted by Jansen.

In this chapter, the combined approach discussed in Section 1.0 is formulated based upon the empirical analysis of average stochastic forces along the column. It has been successfully utilized to explain of the structure of electron stochastic interactions.

Section 6.1 presents the result for the structure of stochastic interactions in a probe-forming beam with a crossover and investigates how this structure affects the final beam blur. The stochastic interactions in a homocentric parallel beam are discussed in Section 6.2. Section 6.3 compares the two above configurations and explains why they produce the same beam blur regardless of a considerable difference in electron densities. The formulation of the model not only gives physical insight into this result, but also makes general predictions beyond those of Jansen's. These predictions are later confirmed in simulations. Section 6.4 briefly discusses the stochastic interactions in beam projection systems.

6.1. Stochastic interactions in a probe-forming beam with a crossover

6.1.0. Stochastic force upon a single electron

Figure 6-2 shows a probe-forming system with a crossover in the middle. Simulation was used to track the transverse stochastic forces F_{x5} and F_{y5} caused by the five nearest neighbors upon an arbitrary electron. Figure 6-3 plots these forces as electron traveled through the region between the two lenses.

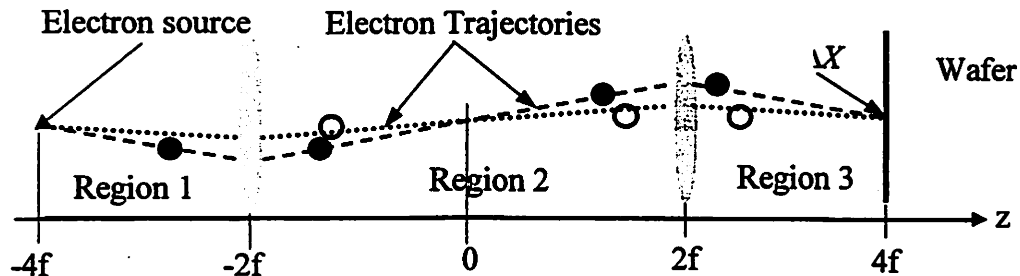

Figure 6-2. Schematic diagram of the simulated beam configuration with a crossover. Accelerating voltage $V=100\ kV$, $\delta V=15V$, beam current $I=1\mu A$, focal length $f=50mm$, and illumination convergence Gaussian semi-angle $\alpha=1.5mR$.

As electron A (dot) passes the crossover, its neighboring electron B (circle) switches from one side of A to the other side, causing the transverse stochastic force to change sign. The symmetry of the transverse forces around the crossover in Figure 6-3 indicates that stochastic Coulomb interactions are small, and that a first order perturbation theory can be applied for its analysis. The symmetry of the forces will cancel

out the blur contribution caused by velocity shift only while the blur caused by trajectory shift survives.

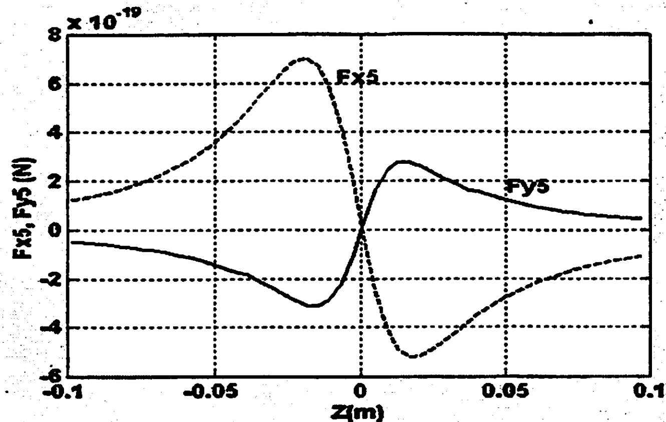

Figure 6-3. Stochastic forces upon an electron as it travels through the region between the two lenses. These forces are computed with five nearest neighboring electrons.

The symmetry of stochastic forces must be distinguished from the space charge effect, which also results in symmetric force patterns in a beam configuration with a crossover. The space charge effect is a macroscopic effect, independent of the microscopic stochastic distribution of the electrons. It depends only on the global distribution of the electrons in the beam column. The stochastic effect however, only depends on the microscopic stochastic distribution of the neighboring electrons.

6.1.1. Averaged stochastic force

In addition to the stochastic forces upon an individual electron, one is also interested in averaging the stochastic forces upon different electrons as they travel through the beam column. In order to characterize the averaged stochastic force, Coulomb interactions were turned on only in a thin region [z, $z+dz$] for one simulation run, as shown in Figure 6-4. This is another application of the special options discussed in Chapter 2. The assumption is that each electron experiences a constant stochastic force as it travels through this thin region. The assumption is appropriate because the relative positions of the electrons take very minor changes in such a short period.

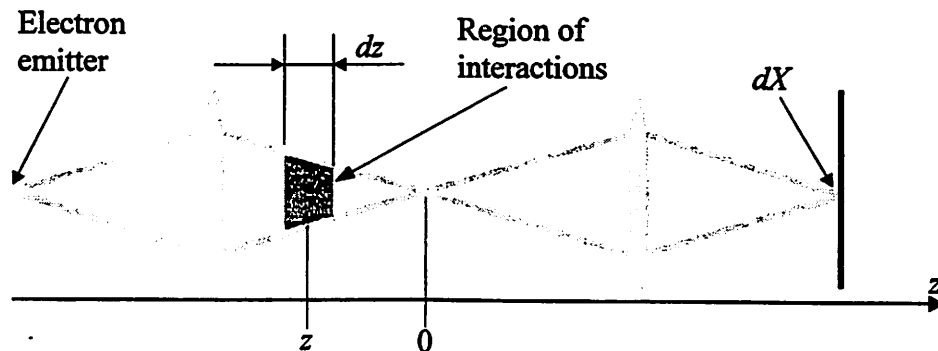

Figure 6-4. The average stochastic forces are measured in simulations. Accelerating voltage is V=100 kV, δV=15V, beam current is I=1μA, focal length is f=50mm, and illumination convergence Gaussian semi-angle is α =1.5.

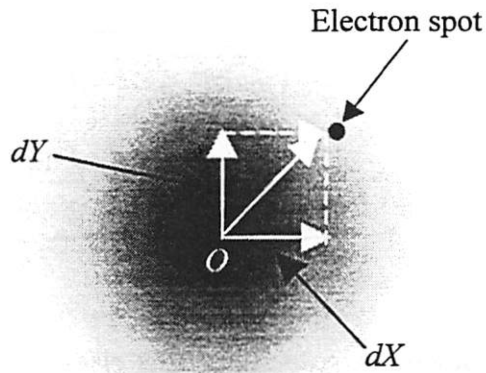

Figure 6-5. Measuring the displacement of an arbitrary electron on the wafer.

For an arbitrary electron, a simple geometrical argument shows that the final displacement in the *x*-direction on the wafer (Figure 6-5) is

Equation 6-1

$$X = x_2 + \left(\frac{v_{x2}}{v_z} - \frac{x_2}{f}\right) \cdot 2f = -x_2 + \frac{v_{x2}}{v_z} \cdot 2f$$

Here x_2 and v_{x2} are the displacement and the velocity of the electron passing through lens 2, f is the focal length of both lenses, and v_z is the axial velocity. The second term in Equation 6-1 is the displacement change on the wafer caused by the action of lens

2. The position shift dX caused by stochastic Coulomb interactions in the region of interaction dz is

Equation 6-2

$$
\begin{aligned}
dX &= -dx_2 + \frac{2f}{v_z} \cdot dv_{x2} \\
&= -dx_2 + \frac{2f}{v_z} \cdot \frac{F_x(z)}{\gamma \cdot m} \cdot \frac{dz}{v_z}
\end{aligned}
$$

where $F_x(z)$ is the stochastic force upon this electron measured in LAB frame. dx_2 and dv_{x2} are the trajectory and velocity shifts at lens 2. γ is the Lorentz factor, m is the electron mass, and dz / v_z is the time to pass through this thin region.

The special options of BEBS also allow us to reposition each electron when it passes lens 2 such that $dx_2 = 0$. This results in a displacement dX that is directly proportional to $F_x(z)$:

Equation 6-3

$$
dX = \frac{2f}{v_z^2} \cdot \frac{dz}{m} \cdot F_x(z)
$$

Average both sides of the equations over all the electrons in the region, and one can concludes that the average stochastic force is proportional to the spot size and therefore can be directly measured through simulations:

Equation 6-4

$$
\langle |F_x(z)| \rangle \propto \langle |dX| \rangle \propto Spot\ size
$$

The spot size is measured for each *4mm* long interaction region along the beam column. The inverse of the beam blur is plotted against the axial position z in Figure 6-6.

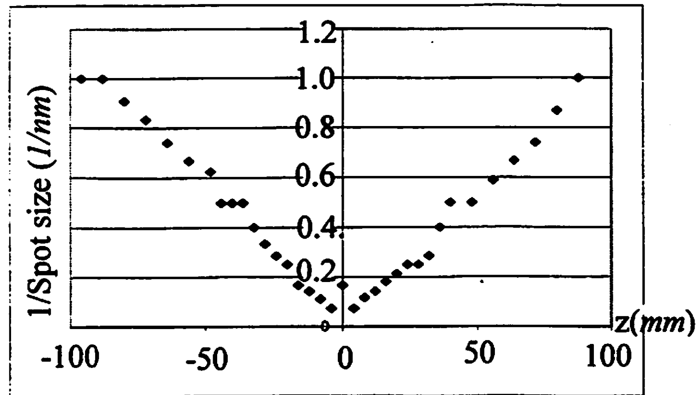

Figure 6-6. Inverse of the spot size versus the axial position of the region of interaction.

The linear relation in Figure 6-5 indicates that spot-size(z) is inversely proportional to z except in the region around the crossover. Thus, the average force

Equation 6-5

$$\langle |F_x(z)| \rangle = \frac{k}{|z|}, \quad z \neq 0$$

where the forces are still finite as the electron density is finite. Here k is a constant independent of z.

The relation in Equation 6-4 is derived for region 2. Yet, a similar argument and result can be applied to region 1 and region 3 as long as the origin of the z-axis is moved to the location of the emitter or the location of the wafer. The constant k, however,

remains unchanged only if the convergence angles in region 1 and 3 are the same as the crossover angle in region 2.

6.1.2. Blur contribution along the optical axis

The beam blur contributions along the optical axis can be characterized by the corresponding averaged stochastic forces. In Equation 6-2, consider the contribution caused by the trajectory displacement in region *dz*,

Equation 6-6

$$dx_2 = dv_x \cdot T = a \cdot dt \cdot T = \frac{Fx(z)}{\gamma \cdot m} \cdot \frac{dz}{v_z} \cdot \frac{(2f - z)}{v_z}$$

where dv_x is the velocity change caused by interactions in region *dz* and *T* is the time for the electron starting from this thin region to reach lens 2. Therefore,

Equation 6-7

$$dX = -\frac{Fx(z)}{\gamma \cdot m} \cdot \frac{dz}{v_z} \cdot \frac{(2f - z)}{v_z} + \frac{Fx(z)}{\gamma \cdot m} \cdot \frac{2f}{v_z} \cdot \frac{dz}{v_z} = \frac{Fx(z) \cdot z}{\gamma \cdot m} \cdot \frac{dz}{v_z^2}$$

In other words:

Equation 6-8

$$\frac{dX}{dz} = \frac{Fx(z)}{\gamma \cdot m} \cdot \frac{z}{v_z^2}, \quad z \neq 0 \quad and \quad X(z = -d) = 0$$

The boundary condition comes from the assumption that Coulomb interactions only occur in the region between the two lenses where $-d \le z \le d$. Now we will prove that

Equation 6-9

$$\frac{d\langle|X|\rangle}{dz} = \frac{\langle|F_x(z)|\rangle}{m} \cdot \frac{|z|}{v_z^{\,2}}, \quad z \neq 0$$

Figure 6-3 shows that $F_x(z)$ only changes its sign at the crossover where $z=0$. Therefore the proof can be shown in two separate cases.

Case 1: $F_x(z) \cdot z \geq 0$

Hence, $\dfrac{dX}{dz} \geq 0$ *owe to Equation* 4 – 7,

$X(z) \geq 0 \quad (-d \leq z \leq d)$ *due to the boundary condition.*

Thus, $|X| = X$.

Take the absolute value of Equation 4 – 7 *on both sides, one obtains*

$$\frac{d|X|}{dz} = \frac{|F_x(z)|}{m} \cdot \frac{|z|}{v_z^{\,2}}$$

Take the ensemble average on both sides:

$$\frac{d\langle |X| \rangle}{dz} = \frac{\langle |F_x(z)| \rangle}{m} \cdot \frac{|z|}{v_z^{\,2}}$$

Case 2: $F_x(z) \cdot z \leq 0$

$|X| = -X$.

$$\frac{d\langle |X| \rangle}{dz} = \frac{\langle |F_x(z)| \rangle}{m} \cdot \frac{|z|}{v_z^{\,2}}$$

Insert Equation 6-4 into Equation 6-8, one obtains:

Equation 6-10

$$\frac{d\langle |X| \rangle}{dz} = \begin{cases} \dfrac{k}{m} \cdot \dfrac{1}{v_z^{\,2}} = const, & -d \leq z \leq d \text{ and } z \neq 0 \\ 0, & z = 0 \end{cases}$$

This result indicates that different regions along the axis make nearly uniform contributions to the final stochastic beam blur in spite of different electron densities. As a matter of fact, the crossover region makes the smallest blur contribution in spite of its high electron density. This result is depicted in Figure 6-7. The area of the shaded region represents the beam spot size while the profile of the region gives the relative contribution from different axial regions.

The relation in Equation 6-10 is derived for region 2. Yet, a similar argument and result can be applied to region 1 and region 3 in Figure 6-2 as long as the origin of the *z*-axis is moved to the location of the emitter or the location of the wafer. The constant *k*, however, remains unchanged only if the convergence angles in region 1 and 3 are the same as the crossover angle in region 2. In general,

Equation 6-11

$$X = X_1 + X_2 + X_3$$

where X_1, X_2, and X_3 are the displacement changes on the wafer caused by interactions in the three regions respectively.

For a thin region of interaction in region 1:

Equation 6-12

$$dX_1 = -dx_2 + \frac{2f}{v_z} \cdot dv_{x2}$$

where dx_2 and dv_{x2} are still the displacement and velocity changes at lens 2 but they are caused by interactions in dz of region 1 instead of region 2. Simple geometrical arguments show that:

Equation 6-13

$$dx_2 = -3dx_1 + \frac{4f}{v_z} \cdot dv_{x1},$$
$$dv_{x2} = dv_{x1} - \frac{v_z}{f} \cdot dx_1$$

where dx_1 and dv_{x1} are the displacement and the velocity changes at lens 1 due to the interactions in thin region dz . Substitute Equation 6-13 into Equation 6-12, and one obtains:

Equation 6-14

$$dX_1 = -(-3dx_1 + \frac{4f}{v_z} \cdot dv_{x1}) + \frac{2f}{v_z}(dv_{x1} - \frac{v_z}{f} dx_1)$$
$$= dx_1 - \frac{2f}{v_z} \cdot dv_{x1}$$

Using the same argument as the one used in the derivation of Equation 6-10, it can be shown that

Equation 6-15

$$\frac{d\langle |X_1| \rangle}{dz} = \begin{cases} \frac{k}{m} \cdot \frac{1}{v_z^{\ 2}} = const, & -2d < z \leq -d \\ 0, & z = -2d \end{cases}$$

In the above derivation, we have used the fact that k remains the same for region 1 as it shares the same beam angle as region 2. Similarly,

Equation 6-16

$$\frac{d\langle|X_3|\rangle}{dz} = \begin{cases} \frac{k}{m} \cdot \frac{1}{v_z^2} = const, & d \le z < 2d \\ 0, & z = 2d \end{cases}$$

The differential blur contributions in all three regions are depicted in Figure 6-7. Notice that the regions near the electron source or the wafer make little blur contribution similar to the crossover region.

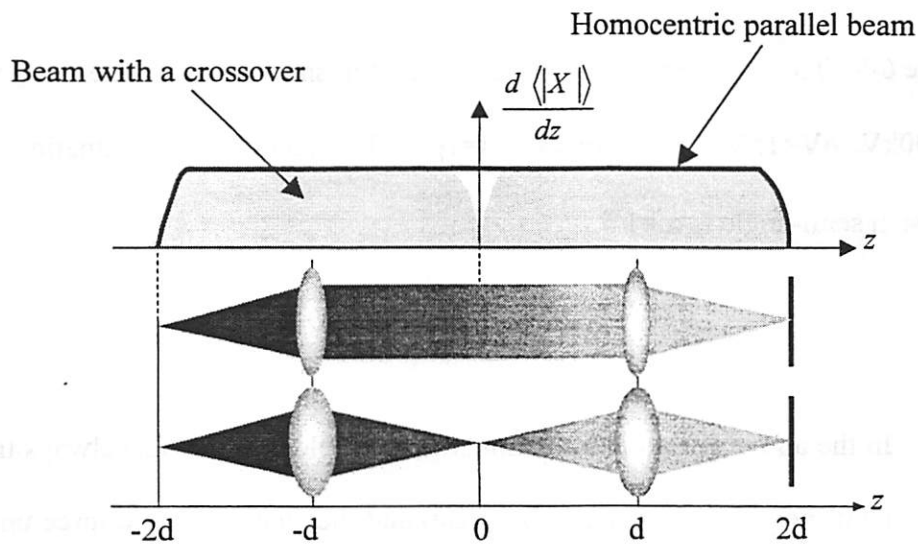

Figure 6-7. Beam-blur contributions along the optical axis for a crossover beam and a homocentric parallel beam that share the same beam angle.

6.2. Stochastic interactions in a homocentric parallel beam

Figure 6-8 shows a homocentric parallel beam column. Again, simulation is used to track the transverse stochastic forces F_{x5} and F_{y5} upon an arbitrary electron as it travels through the region between the two lenses. The result is visualized in Figure 6-9.

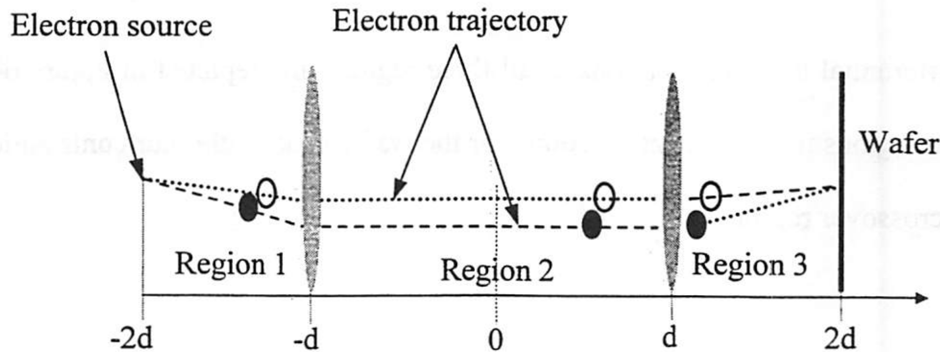

Figure 6-8. The homocentric parallel beam used in simulation. Accelerating voltage is V=100kV, δV=15V, beam current is I=1μA, d=100mm, and illumination convergence Gaussian semi-angle is α =1.5.

In the above beam configuration, however, electron A (dot) always travels on the same side of neighboring electron B (circle) and thus the stochastic force upon A caused by B does not change its sign. Figure 6-9 shows that the stochastic force upon an arbitrary electron is nearly constant. Thus, the average force $F_x(z)$ is also constant along the z-axis. Similar to Equation 6-1, one can obtain the displacement X' on the wafer if the Coulomb interactions are only switched on in region 2:

Equation 6-17

$$X' = x_2 + \left(\frac{v_{x2}}{v_z} - \frac{x_2}{f} \right) \cdot f$$
$$= \frac{v_{x2}}{v_z} \cdot f$$

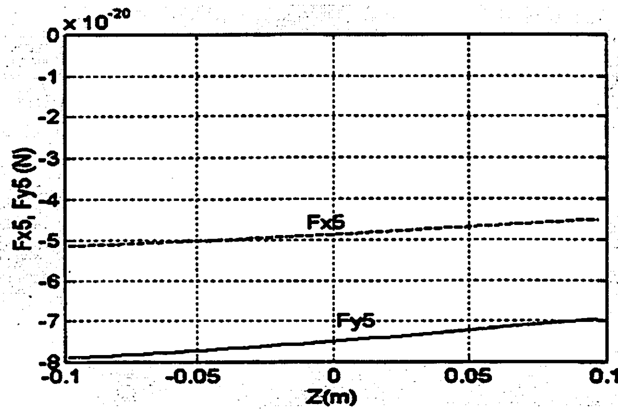

Figure 6-9. Stochastic forces upon an arbitrary electron as it travels through region 2. The forces are computed with the five nearest neighboring electrons.

Analogously to the derivation of Equation 6-7 and Equation 6-8, one obtains

Equation 6-18

$$\frac{dX'}{dz} = \frac{F_x}{\gamma \cdot m} \cdot \frac{f}{v_z^2}$$

Equation 6-19

$$\frac{d\langle |X'| \rangle}{dz} = \frac{\langle |F_x| \rangle}{\gamma \cdot m} \cdot \frac{f}{v_z^2} = const, \quad -d \le z \le d$$

The analysis of region 1 and 3 are similar to that of the crossover beam and the expressions are the same as Equation 6-15 and Equation 6-16. Thus, the blur contribution is nearly uniform except in the regions near the electron source and the wafer. It can be shown that this constant is the same as the constant in the crossover beam as long as the two configurations share the same beam angle. The result is visualized in Figure 6-7.

6.3. Other probe forming beam configurations

The model used in the above analysis can be applied to other probe-forming beams as well. As an example, this model predicts that the three beam columns in Figure 6-10 produce the same beam blur as long as the beam angle α remains constant. The distance between the two lenses is always *L/2* as a result of constant beam angle. This prediction has been confirmed with simulations. The blur is *42nm* at beam current $I=1\mu A$.

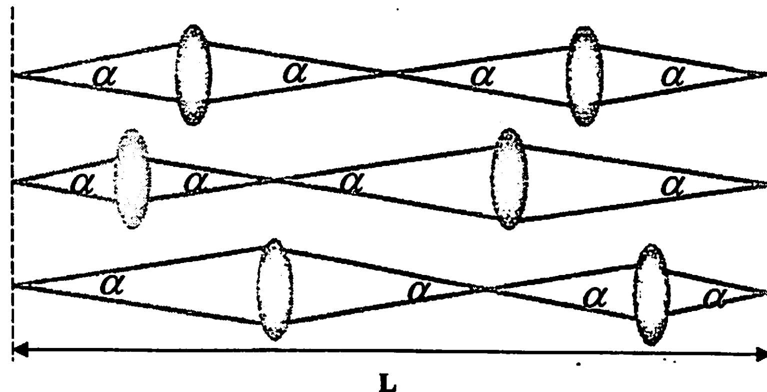

Figure 6-10. Three beam configurations with the same column length and the same beam angle. $V=100\ kV$, $\delta V=15V$, $L=400mm$, and Gaussian semi-angle $\alpha=1.5$.

6.4. Stochastic interactions in a system with multi-emitter array

The *4X* demagnification system used in this study is the same as the one in Figure 2-1. The mask has a *5X5* array of emitters with *200μm* spacing. The structures of the stochastic forces are more complicated in a high throughput beam system. In Figure 6-11, electrons A (circle) and B (dot) emitted from the same region on the mask travel through the column similarly to the case of the homocentric parallel beam. This result challenges Mkrtchyan's assumption of random correlation length [6], in which the nearest neighbor electron of the test particle does not change. Electron C (triangle), however, changes its relative position with respect to A and B. Moreover, the electron trajectories actually cross at different positions along the *z*-axis, in contrast to a probe-forming beam with a crossover where all the trajectories cross around the same point.

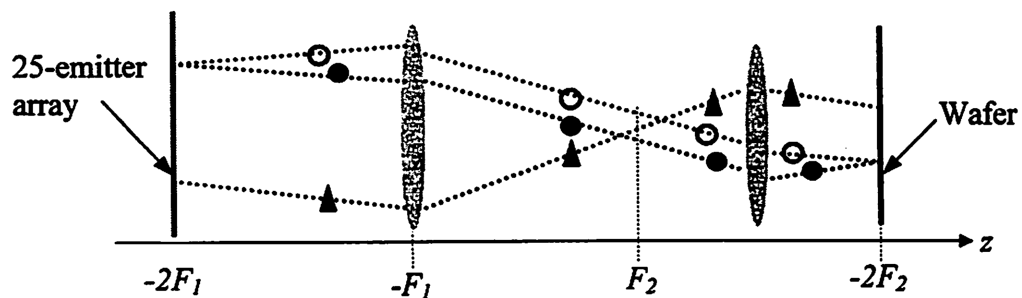

Figure 6-11. The relative positions of the electrons in a system with a 25-emitter array. Accelerating voltage is $V=100\ kV$, $\delta V=15V$, beam current is $I \doteq 1\mu A$, focal lengths are $F_1=160mm$ and $F_2=40mm$, and illumination convergence Gaussian semi-angle is $\alpha=1.5$.

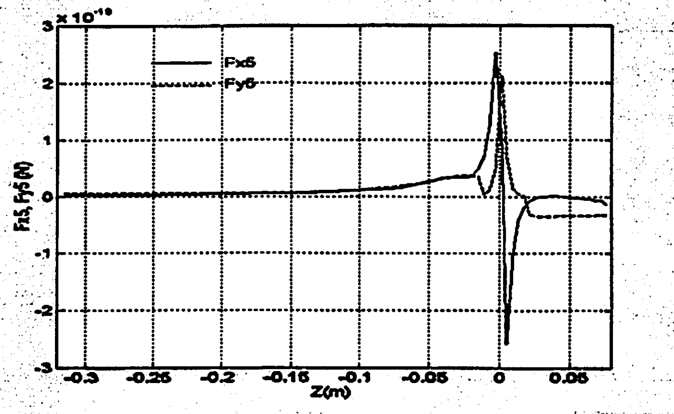

Figure 6-12. Stochastic forces upon an electron as it travels through the beam projection column. The forces are computed with five nearest neighboring electrons. Beam current $I=1\mu A$.

Figure 6-12 shows the transverse stochastic forces F_{x5} and F_{y5} upon an electron that is emitted from a region near the edge of the projection field. This electron does not encounter any neighboring crossing electrons emitted from other regions until it comes near the crossover region where components of the force change signs. In comparison with the crossover beam in the previous section, the neighboring electrons cross at different locations in a multi-emitter array system. Thus the stochastic force patterns are not strongly symmetric around $z=0$. Due to the irregular pattern of the stochastic forces, the algebraic model developed in the previous sections has yet to be extended to the quantitative analysis of the multi-emitter system.

6.5. Conclusions

The structures of stochastic Coulomb interactions have been revealed both in probe-forming beams and in multi-spot projection electron beam columns. A technique combining an algebraic approach and simulations has been developed for the analysis and comparison of the stochastic Coulomb interactions and the stochastic blur. It has been shown that in a crossover configuration where the beam angles are equal, the blur contribution is nearly constant along the column, very similar to a parallel beam. The randomized correlation length assumption of Mkrtchyan's Nearest Neighbor Theory needs modification to include symmetry around the crossover. The simulation shows that the randomized correlation length is a function of the beam diameter and that correlated interactions occur at other axial positions due to symmetry with respect to the beam crossover. Further study is needed to investigate the possibility of reducing the stochastic blur through manipulating its rich structures.

7 Scaling Laws of Stochastic Coulomb Interactions

7.0. Introduction

The previous chapter presented a combined approach to study the beam blur contribution along the optical axis. Nevertheless, this method is no longer applicable if one wants to rescale an electron beam system and compare the blur sizes. In contrast to the space charge effect, the theoretical analysis of the stochastic effect is much more sophisticated. Different theoretical models have been developed to predict the beam blur caused by the electron-electron stochastic interactions in various beam configurations. These theories, which are briefly introduced in Chapter 2, are based on a series of unverified assumptions or approximations. Heretofore in simulation studies the stochastic blur contributions have always been convolved with those of the space charge and can only be isolated through approximation. This section describes a stochastic effect simulator that directly measures the stochastic blur.

Figure 7-1 shows the schematic diagram of the stochastic effect simulator. BEBS use moving positrons to eliminate the space blurs. A positron has the same mass but opposite charge as an electron. In the simulation, the positrons in the column share the

same energy, energy spread, and spatial distribution as the electrons. Therefore, the global space charge effect is completely eliminated and the beam blurs are only caused by the stochastic interactions among the electrons and the positrons. The positrons exert and experience similar stochastic forces to their electrons counterparts and produce the beam blur together with the electrons. As an example, the total beam blur created by the combining of a *15μA* electron beam and a *15μA* positron beam will be the same as the stochastic blur produced by a *30μA* electron beam.

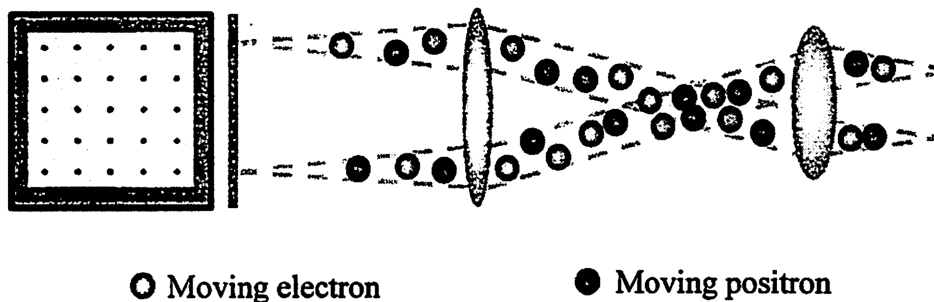

O Moving electron ● Moving positron

Figure 7-1. Schematic diagram of the stochastic effect simulator.

This stochastic effect simulator can directly measure the stochastic blurs in any beam configurations. The space charge blurs can be easily obtained from the following relationship:

Equation 7-1

$$\text{space charge blur} = \sqrt{\text{total blur}^2 - \text{stochastic blur}^2}$$

7.1. Theory

This section provides a preliminary proof of the validity of the stochastic effect simulator. Figure 7-2 shows the cross sections of two identical beam columns A and B, one for an ordinary electron beam simulator and the other for the corresponding stochastic effect simulator. Assume that the particle locations in either of the columns follow identical and independent distributions. Two test electrons are at identical positions of the two columns as shown in the figure. F_x, F_y, F^*_x and F^*_y are the total forces upon them caused by other electrons in the column. Now we claim:

Equation 7-2 $$Variance(F_x) = Variance(\widetilde{F}_x)$$

Equation 7-3 $$Variance(F_y) = Variance(\widetilde{F}_y)$$

Without losing generality, it is sufficient to show:

Equation 7-4 $$E(F^2) - E^2(F) = E(\widetilde{F}^2)$$

Remember that $E(\widetilde{F}) = 0$ due to the effect of positrons. Here $F = \sum_{i=1}^{N} F_i$, $\widetilde{F} = \sum_{i=1}^{N} \widetilde{F}_i$, where F_i and $\widetilde{F}_i$ are the forces caused by particle i in the respective columns. Moreover, all the F_is follow the same statistical distribution, i.e., $f(F_i) = f(F_j)$, $f(\widetilde{F}_i) = f(F_j)$ if particles i is positive and $f(-\widetilde{F}_i) = f(F_j)$ if particles i is negative.

In order to show Equation 7-4, we first show

Equation 7-5 $$E\left((F_1 + F_2)^2\right) - E^2(F_1 + F_2) = E\left((\widetilde{F}_1 + \widetilde{F}_2)^2\right),$$

where particle 1 and 2 carry opposite charges in the stochastic effect simulator column B.

$$\begin{aligned} LHS &= E\left(F_1^2 + F_2^2 + 2\cdot F_1\cdot F_2\right) - E^2(F_1) - E^2(F_2) - 2\cdot E(F_1)\cdot E(F_2) \\ &= 2\cdot Var(F_1) \end{aligned}$$

$$\begin{aligned} RHS &= E\left((F_1 - F_2)^2\right) = E\left(F_1^2 + F_2^2 - 2\cdot F_1\cdot F_2\right) \\ &= E\left(F_1^2\right) + E\left(F_2^2\right) - 2\cdot E(F_1)\cdot E(F_2) - E^2(F_1) - E^2(F_2) + E^2(F_1) + E^2(F_2) \\ &= 2\cdot Var(F_1) \\ &= LHS \end{aligned}$$

Now, all the particles with opposite charges in column B can be paired. Similarly, all the electrons in column A are also paired. Each pair of particles produces a total force, which conforms to similar independent distribution in two columns. Analogous to the derivation of Equation 7-5, it can be shown that $E\left(F^2\right) - E^2(F) = N\cdot Var(F_1) = E\left(\tilde{F}^2\right)$.

Remember that the position of the test electron in each column is arbitrary. The variance of the force is actually a good measurement of the magnitude of the stochastic force. Hence, the stochastic forces at identical positions in the two columns are roughly equal. Therefore, the stochastic effect simulator produces the same stochastic blur as the original electron beam column.

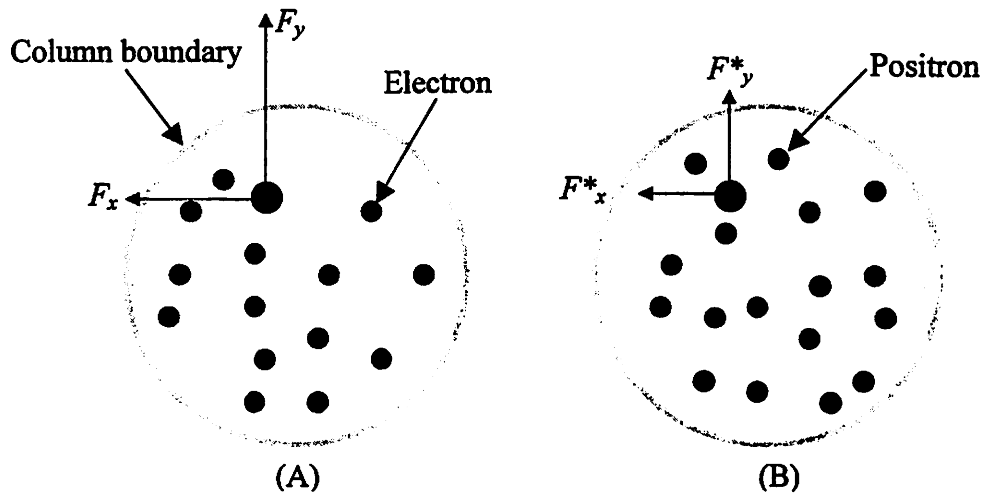

Figure 7-2. Cross sections of an ordinary electron beam simulator A and the corresponding stochastic effect simulator B.

7.2. Scaling laws

7.2.0. Comparison with Jansen's Theory

Jansen's theory [26] predicts the scaling of the stochastic beam blur versus the beam current for a SCALPEL system:

Equation 7-6 $$\textit{Jansen's stochastic blur} \propto I^{0.67}$$

Simulation with BEBS shows that:

Equation 7-7 $$\textit{BEBS's stochastic blur} \propto I^{0.62}$$

The simulation results roughly agree with Jansen's prediction. Nevertheless, the spot size is larger than Jansen's prediction at each current as shown in Figure 7-3. Jansen made a series of approximations and assumptions, which includes: (1) each electron only being involved in one or no strong collisions in a beam segment, and (2) the interactions being fully correlated in one beam segment and fully uncorrelated between beam segments. These approximations all contribute to the above discrepancy.

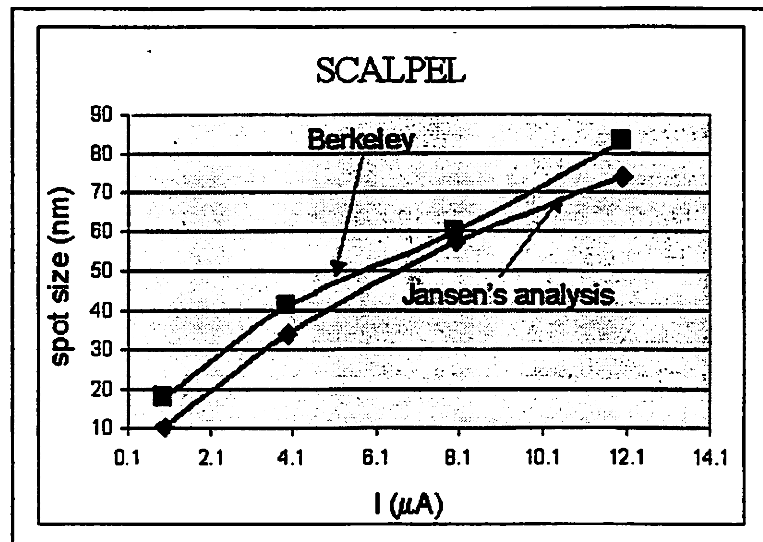

Figure 7-3. Comparison between the stochastic blur measured with BEBS and the blur from Jansen's prediction.

7.2.1. Scaling laws for a 25-emitter array system

The applications of Jansen's theoretical model are restricted by the beam configurations due to its complexity. The stochastic effect simulator, however, can be

easily applied for different beam geometries. In this section, the scaling laws are developed for the 4X demagnification 25-emitter array system shown in Figure 7-1.

The spot sizes are plotted against beam current, beam energy, emitter spacing, column length and beam convergence angle in Figure 7-4, 7-5, 7-6, 7-7, and 7-8 respectively. The space charge blurs are calculated based on Equation 7-1.

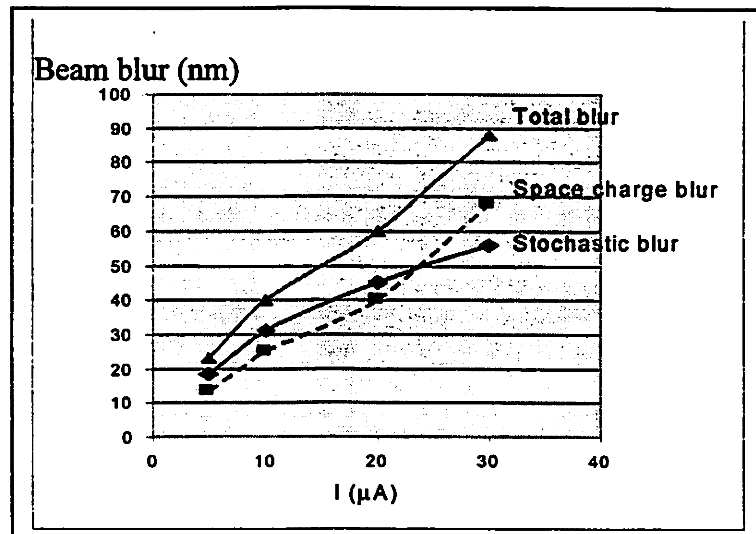

Figure 7-4. Current dependency of the beam blurs in a 25-emitter array system.

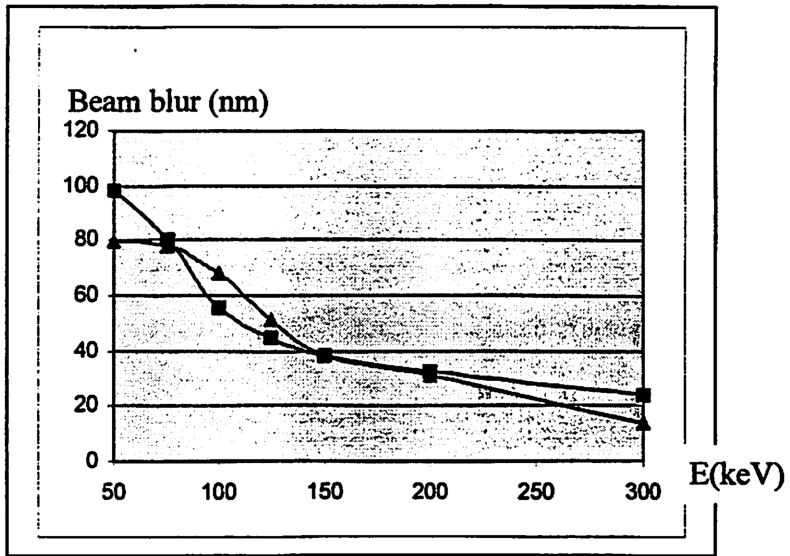

Figure 7-5. Beam energy dependency of the stochastic blur and the space charge blur.

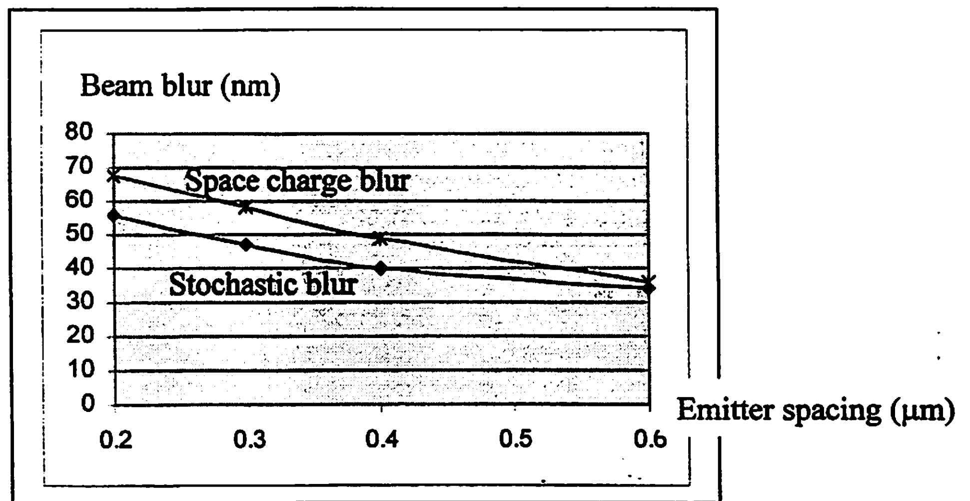

Figure 7-6. Emitter spacing dependency of the stochastic blur and the space charge blur.

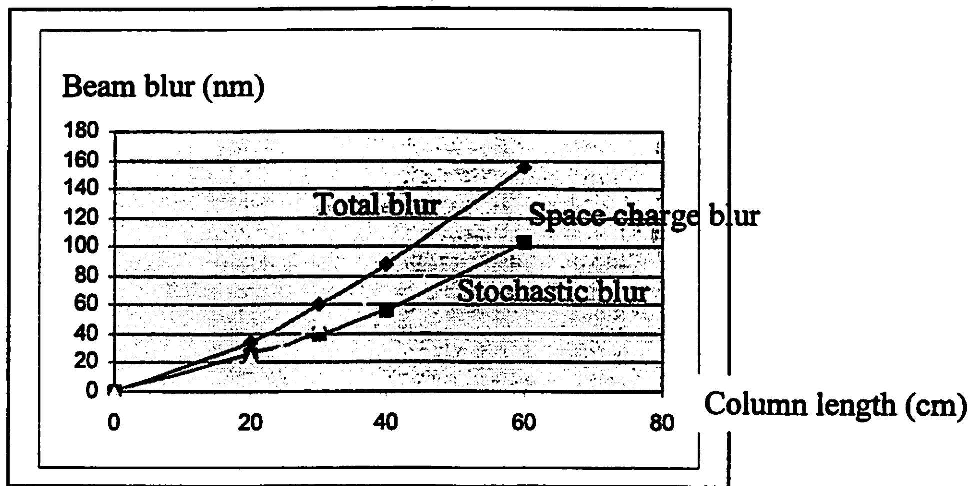

Figure 7-7. Column length dependency of the stochastic blur and the space charge blur.

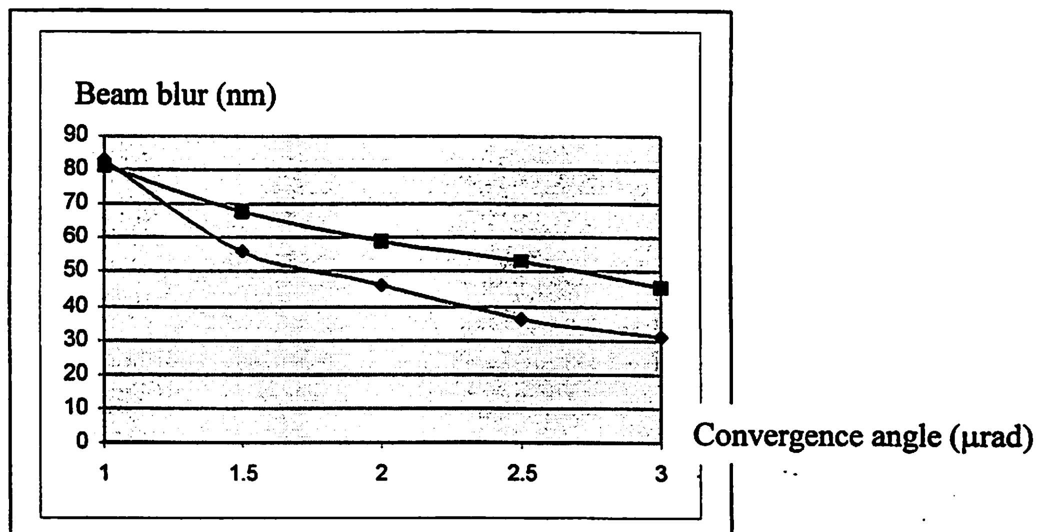

Figure 7-8. Convergence angle dependency of the stochastic blur and the space charge blur.

The above curves lead to the scaling laws for the stochastic blur and the space charge blurs:

Equation 7-8 $$\text{Stochastic blur} \propto I^{0.62} L^{1.27} \alpha^{-0.9} S^{-0.45} V^{-2/3}$$

Equation 7-9 $$\text{Space charge blur} \propto I^{0.62} L^{1.43} \alpha^{-0.6} S^{-0.58} V^{-2/3}$$

Here I is beam current, L is column length, α is illumination convergence angle, S is emitter spacing, and V is beam voltage. The blur size is independent of the beam energy spread ΔE when it is within 15eV. The scaling laws for the space charge blurs agree with Han's theoretical predictions [42].

8 Impact of Positive Ions and Effect of Lens Aberrations

8.0. Introduction

The aberrations induced by the lensing action of global space charge of the electrons result in beam blur that increases with beam current, as first demonstrated by Han *et al* [3]. There are a lot of papers which deal with space charge neutralizations in various systems such as cathode ray tube (CRT) and focused ion beams [45] [47]. However, it is not clear whether the neutralization scheme would be effective for the high throughput e-beam due to the light mass of electrons. Xiu [30] [31] studied the effect of space charge coils and a multi-pole projector in electron beam columns and tried to reduce field curvature and on-axis aberrations. Nevertheless, no quantitative results have been given on the beam blur reductions. This chapter discusses techniques that effectively reduce the space charge effect. Section 8.1 investigates the feasibility of reducing the global space charge with stationary neutralizing ions in electron beam columns. Section 8.2 explores the feasibility of reducing space charge effect with induced lens aberration. The summary and conclusions are given in Section 8.3.

8.1. Impact of positive ions

The beam blur produced in an electron beam system can be decomposed into stochastic blur and space charge blur, which are caused respectively by the stochastic Coulomb interactions and the global space charge effect. Introducing a cloud of positive ions in the electron beam column can reduce the global net charge and thus decrease space charge blur. However, this will cause a considerable increase in stochastic blur contribution due to the increased opportunity for collisions. Changes of the total beam blur depend on the trade-off between these two competing tendencies. The schematic diagram is shown in Figure 8-1.

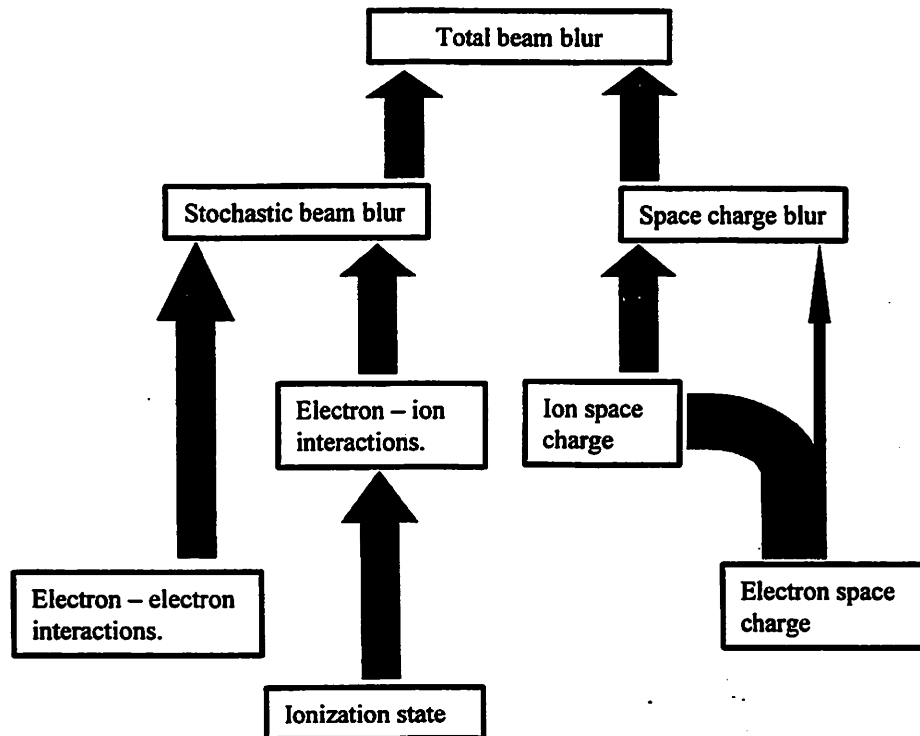

Figure 8-1. Effect of neutralizing ions upon electron beam blurs.

Figure 8-2 shows the simulated multi-emitter array system with both projection electrons and positive ions in the column. The ions are assumed to be stationary compared to fast moving electrons because of their large masses. To find the most favorable configuration, ion distribution *A* and distribution *B* are tested. In configuration *A*, the relation between the ion number densities and the electron number densities are given by:

Equation 8-1 $$f_I(x,y,z) = f_E(x,y,z)/\gamma$$

throughout the beam column. The space charge effect is completely eliminated in this case. γ is caused by the relativistic effect. In configuration *B*, however, ions are introduced only in the region between the two lenses where their distributions follow Equation 1. The space charge effect is partially eliminated here. In our initial studies, each ion is assumed to have only one positive charge (such as H^+).

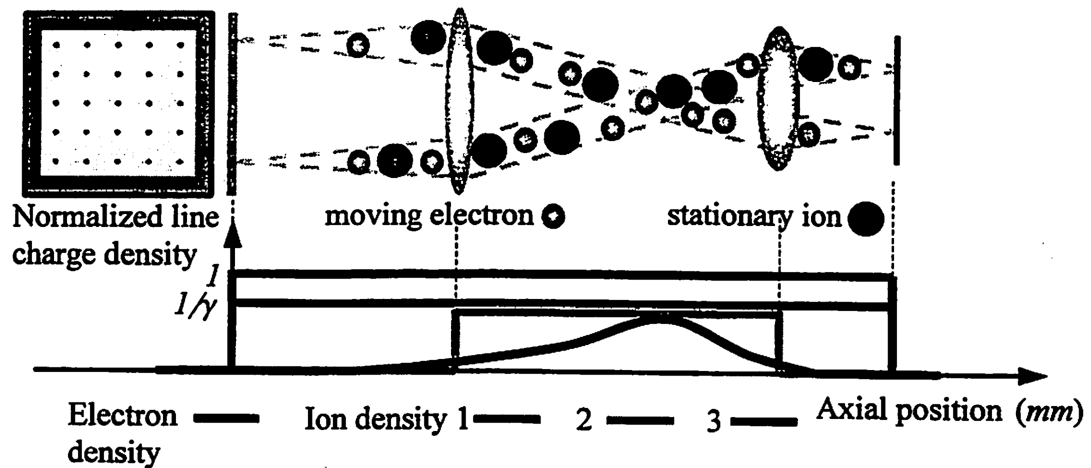

Figure 8-2. Schematic diagram of a high throughout electron beam column with neutralizing ions.

Figure 8-3 shows that the percentage blur reduction increases with the beam current. This is because the space charge blur dominates at higher beam currents as discussed in Chapter 5 and it is more effective to reduce the total beam blur through eliminating the space charge effect. Up to *24%* blur reduction has been achieved at $30\mu A$ with neutralization scheme B. Blur reduction is less effective with neutralization scheme A, especially at beam currents below $15\mu A$. In fact, in the regions outside the two lenses, the stochastic Coulomb interactions dominate over the space charge effect at low beam currents. Introducing ions in these regions in scheme A leads to insignificant reduction of space charge blur but considerable increase of stochastic blur. Other ion distribution schemes have also been extensively studied with simulations, including Gaussian and

Lorentzian distributions along the optical axis. Scheme B gives the best blur reduction found to date.

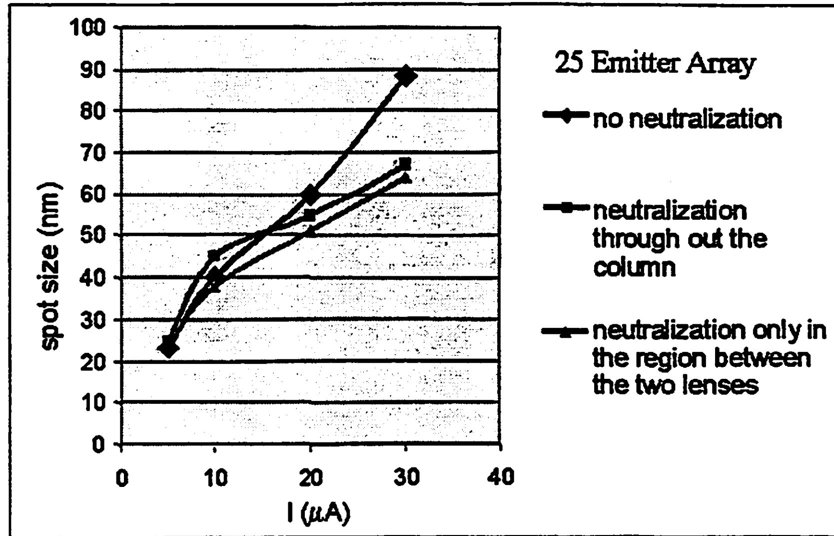

Figure 8-3. Beam current dependency of spot sizes for different neutralization schemes.

Figure 8-4 shows the point spreads on the optimal target plane without neutralizing ions (left) and with neutralization scheme B (right). With the presence of ions, the beam spots near the edge of the field are smaller and much more symmetric. Some residual aberration still appears to be present in the image on the right because only electrons in the region between the lenses are neutralized.

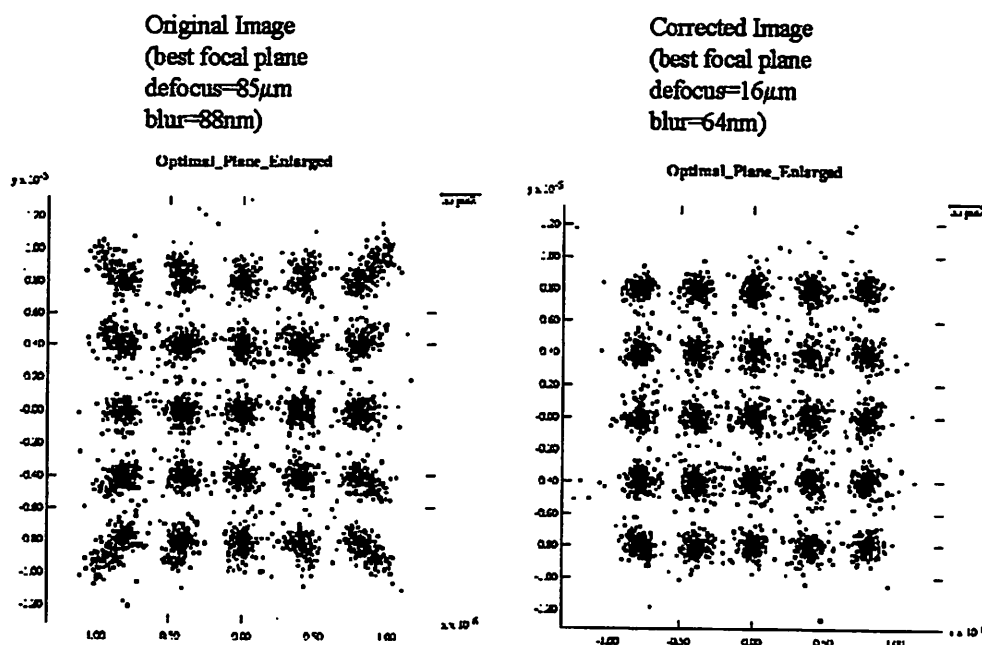

Figure 8-4. The point spreads before and after the correction with neutralizing ions.

The blur reduction also depends on the ionization state of the ions. With ions in a higher ionization state, such as He^{2+}, the ion number density must be decreased in order to maintain the same space charge neutralization. The number of recoils for each electron are decreased due to the smaller number of charge particles in the column. Nevertheless, the magnitude of each recoil tends to increase because each individual ion has more charges. The total stochastic effect depends on the tradeoff between these two competing tendencies. Figure 8-5 illustrates how the beam blur reductions are affected by ionization states. To better understanding the trend, we also simulate the cases of fictitious ions $Fic^{1.5+}$ and $Fic^{0.5+}$ with fractional ionization states. When the ionization state approaches

zero, the statistical ion distribution approaches a continuum of a charged cloud, in which the space charge effect is perfectly eliminated with no increase in stochastic blur. In this case, the spot size approaches the limit of stochastic beam blur, which can be directly measured with our stochastic effect simulator described in Chapter 5.

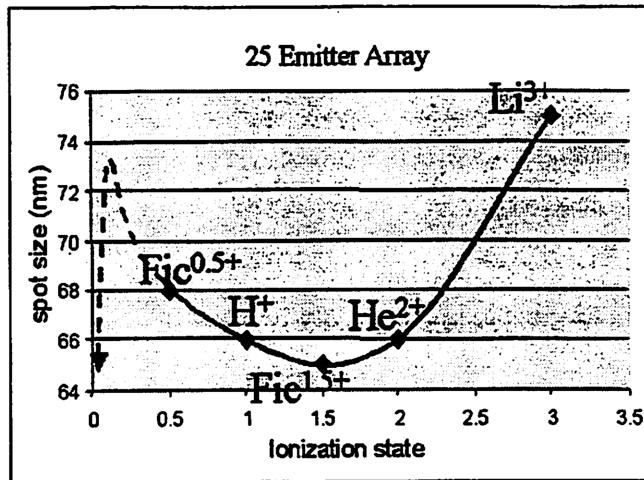

Figure 8-5. Ionization state dependency of the spot sizes. Neutralization scheme *A* is used here for each ionization state. The stochastic beam blur is 56nm as measured in Chapter 8.

8.2. Effect of the lens aberrations

The neutralization technique, however, inevitably increases the stochastic blur. This section investigates the feasibility of reducing the space charge blur through introducing lens aberrations. These induced aberrations are intended to cancel or partially

cancel the aberrations of the space charge lens. Figure 8-6 shows the schematics of such a system.

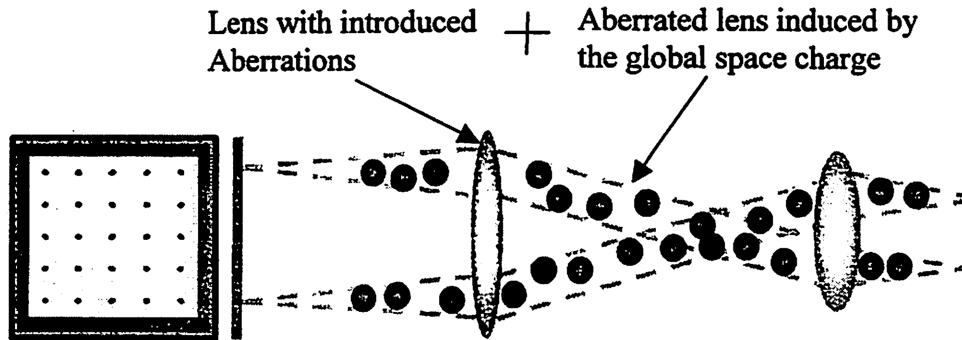

Figure 8-6. Introducing lens aberrations to reduce the space charge blur in a high throughput electron beam system. Only two beamlets are shown for clarity.

The effects of different aberrations have been extensively explored through simulations. Introducing astigmatism in lens 1 so far has led to the best beam blur reduction. Other tested aberrations include field curvature, spherical aberration, distortion, coma, and axial astigmatism. The aberrations used in this thesis work follow the definitions given by Born and Malacara *et al.* in [72] [73]. Figure 8-7 shows that the spot size is minimized with the proper amount of astigmatism of the first projection lens. The astigmatism is defined as

$$D = C_{astig} \cdot r^2 \cdot \theta$$

where r is the radial distance measured on the first projection lens, θ is the incident angle of the electron on the lens, and D is the corresponding position change on the target plane caused by the aberration.

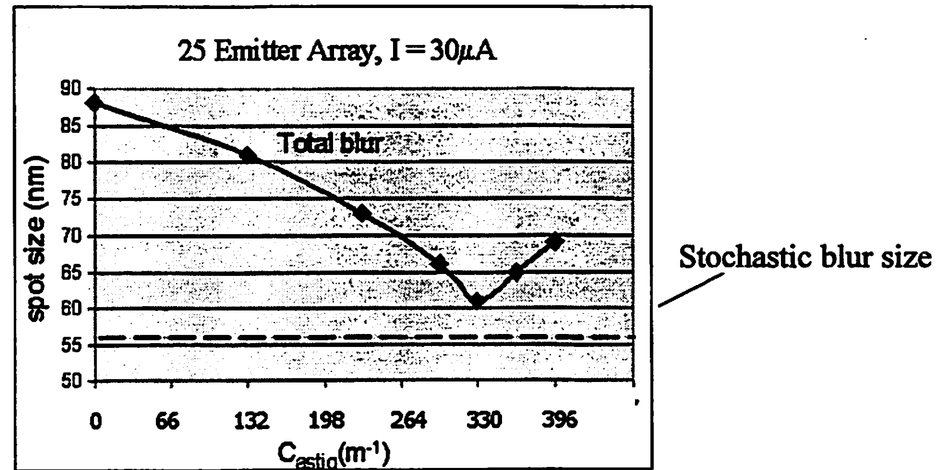

Figure 8-7. Beam blur reduction depends on the magnitude of the induced astigmatism.

The beam spot reaches its minimum of 61nm with 330m^{-1} astigmatism in the first lens. The percentage blur reduction is about 31%. The spot size increases when the astigmatism caused by the space charge effect is either under-compensated or overcompensated. As one can see, the reduced beam blur closely approaches the stochastic blur limit, which is around 56nm. Figure 8-8 shows the point spreads at the best focal plane before and after the correction. The spots near the edge of the field are significantly improved. Similar to neutralizing ions, the blur reduction technique with lens aberrations is more effective at higher beam currents when the space charge blur dominates.

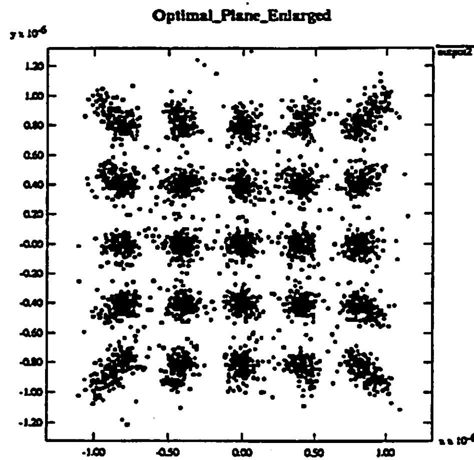

Original image (best focal plane defocus=85μm, blur=88nm)

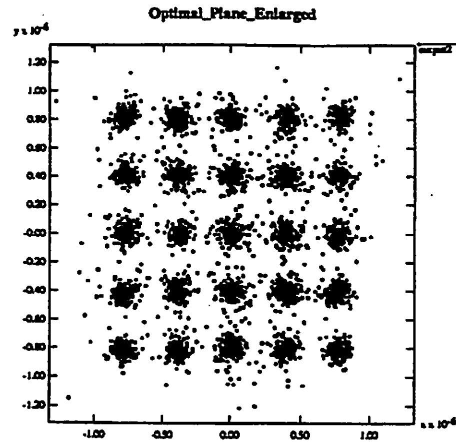

Corrected image (best focal plane defocus=98μm,blur=61nm)

Figure 8-8. The point spreads before and after correction with astigmatism.

8.3. Summary and conclusions

Different beam blur reduction techniques have been explored in simulation with either neutralizing ions or introduced lens aberrations. Blur reductions of *24%* and *31%* have been respectively achieved with the above two schemes at *30μA* beam current and *1.5mR* illumination convergence angle. The percentage reductions are more pronounced at higher beam currents.

9 Electron Interaction with Photo-resist

9.0. Introduction

Since 1960s a series of Monte Carlo models have been proposed and refined to examine the electron interactions with solids. Among these models, the hybrid model was developed by Murata *et al.* [22] to simulate the electron energy deposition in the photo-resist. The hybrid, however, is based on the unverified assumption that all forms of deposited energy contribute equally to the exposure events. The detailed mechanisms of exposure reactions are beyond the scope of this model.

The analytical Electron-Resist Interaction Model (ERIM) developed at UC Berkeley is a recommended approach to study the details of the electron-resist interaction process through reaction cross sections. Section 9.1 gives the schematics of the ERIM. Section 9.2 discusses the secondary electron emission process. Section 9.3 investigates the exposure process using the reaction cross-section approach. All of the components are linked together in Section 9.4 and the algebraic expression describing the spatial distribution of the exposure events is presented.

9.1. Schematics of ERIM

Figure 9-1 shows the schematic diagram of the ERIM model. The high-energy primary electrons are emitted from a point source. Low energy secondary electrons are emitted along the primary electron path and cause most of the exposure events, as will be discussed in later sections. The deflection process of primary electrons caused by elastic scattering can be separated from the secondary electron emission process for the purpose of analysis.

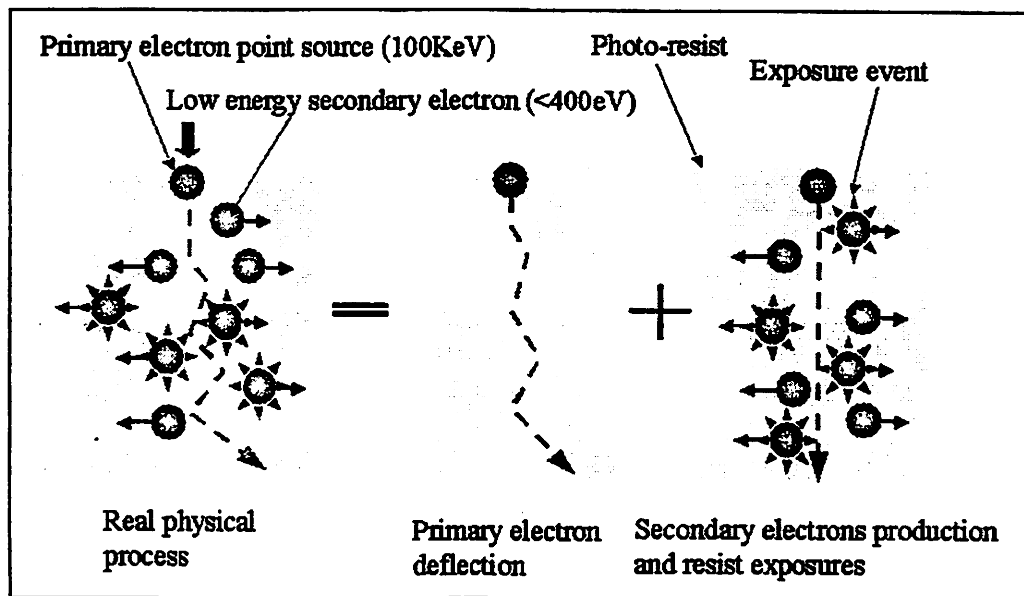

Figure 9-1. Schematic diagram of the secondary electron productions and the exposure process.

The ERIM is a continuous model based on the probability distributions of primary electrons $f_{pr}(E,r,z)$, secondary electrons $f_{se}(E_s,r,z)$, and the spatial distribution of the exposure events $f_{exp}(E,r,z)$ as indicated in Figure 9-2.

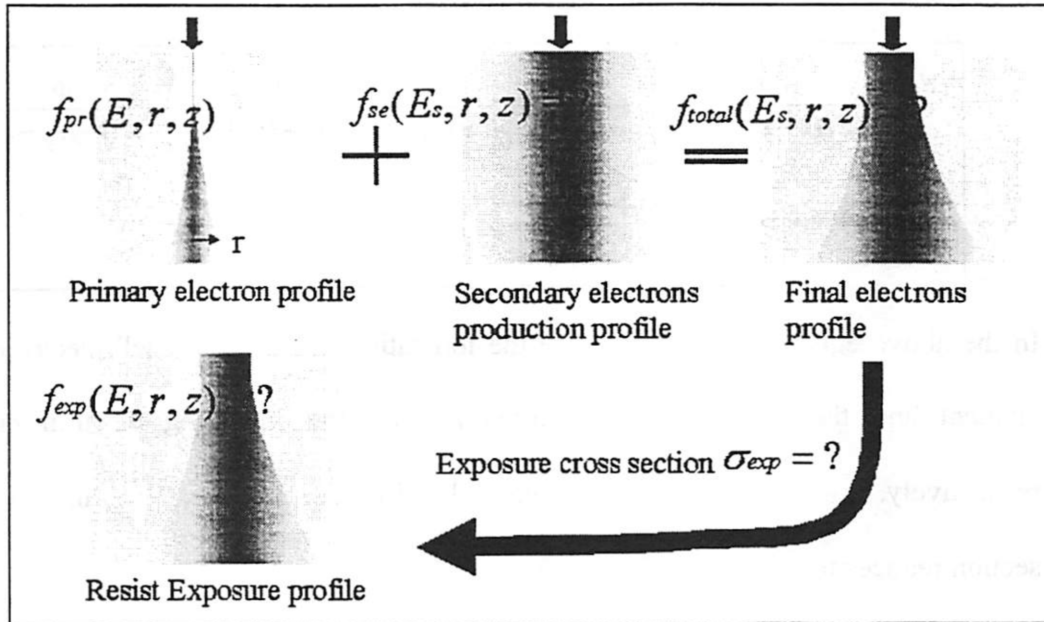

Figure 9-2. Schematic diagram of the continuous ERIM model.

The total exposure profile is the sum of the exposure profiles caused by primary and secondary electrons, respectively. As will be shown in Section 9.3, at a primary beam energy of *100KeV*, secondary electrons are responsible for up to *80%* of the exposure events. Moreover, the angular deflections of the primaries are negligible at such high energy. The exposures by the primaries are roughly along straight trajectories and the resolution limit of exposure events is limited by the spatial distribution of the secondaries.

9.2. Secondary electron emission process

The differential cross section of the secondary electron production is given by Vriens [59] as following:

Equation 9-1

$$\frac{d\sigma_{ij}}{d\varepsilon} \cong \frac{\pi e^4}{E^2(1+2U_{ij})} \cdot \left[\left\{ \frac{1}{\varepsilon^2} + \frac{4U_{ij}}{3\varepsilon^3} \right\} + \left\{ \frac{1}{(1+U_{ij}-\varepsilon)^2} + \frac{4U_{ij}}{(1+U_{ij}-\varepsilon)^3} \right\} - \frac{\Phi}{\varepsilon(1+U_{ij}-\varepsilon)} \right],$$

$$where,\ \Phi = \cos\left\{ -\left(\frac{R_y}{1+U_{ij}} \right)^{1/2} \ln U_{ij} \right\}.$$

In the above equation, U_{ij} and R_y are the ionization energy of j shell electrons of an i element and the Ryberg energy normalized by the incoming electron energy E, respectively. ε is the energy transfer normalized by E. When $E >> U_{ij}$, the above cross section reduces to:

Equation 9-2

$$\frac{d\sigma_{se}}{dE_{se}} \cong \frac{\pi e^4}{E_{pr}} \cdot \frac{E_{se} + \frac{7}{3}J}{(E_{se}+J)^3}$$

where U_{ij} is replaced by the mean ionization energy J which is 74eV for PMMA [74], E_{pr} and E_{se} are the primary and secondary electron energy, respectively.

The total Vriens cross section for PMMA at high beam energy is then given by:

Equation 9-3

$$\sigma_{se} \cong \frac{5}{3} \cdot \frac{\pi e^4}{E_{pr}} \cdot \frac{1}{J} = 1.45 \times 10^{-20} (cm^2)$$

Equations 9-2 and 9-3 clearly indicate that the number of secondary electrons is inversely proportional to the primary electron energy, even though the shape of the curve for secondary electron distribution remains the same. Figure 9-3 plots the number of secondary electrons against the corresponding energies when three thousand *100KeV* primary electrons are incident on a *100nm* thick PMMA resist. The three thousand electrons correspond to the minimum dose of $500\mu C/cm^2$ for $10nm \times 10nm \times 100nm$ PMMA at a beam energy of *100KeV*. The graph shows that *81%* of secondary electrons have energies below *200eV*. The total number of secondary electrons is:

Equation 9-4

$$N_{se} = \sigma_{se} \cdot n_e \cdot l \cdot 3000 = 157$$

Here n_e is the total electron density in PMMA and $l = 100nm$ is the resist thickness.

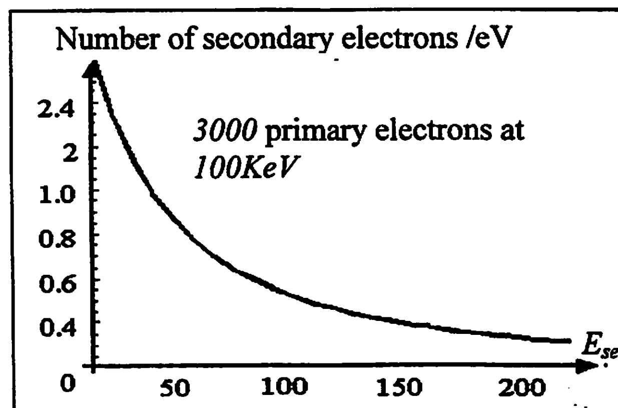

Figure 9-3. Energy dependency of the secondary electron production.

The number of further cascade electrons is less than ten. This number has been evaluated using the secondary electrons at energies of *400eV* or less. The effect of the cascade electrons is not considered in later discussions due to their small number.

The modified Bethe formula by Joy and Luo [60] is used to describe the energy loss of the secondaries along their paths:

Equation 9-5

$$\frac{dE}{ds} \cong -785 \cdot \frac{\rho Z}{EA} \cdot \ln\left[\frac{1.166(E + 0.85J)}{J}\right]$$

where *Z, A* and ρ are the atomic number, atomic weight and density of the photo resist respectively. Figure 9-4 shows that *90%* of the secondary electrons whose energies are below *400eV* can only travel less than *12nm* in PMMA resist. Meanwhile, *81%* of the secondaries whose energies are below *200eV* can only travel less than *5nm*. This agrees with the experimental result that the resolution limit for *100nm* PMMA is around 10nm [75].

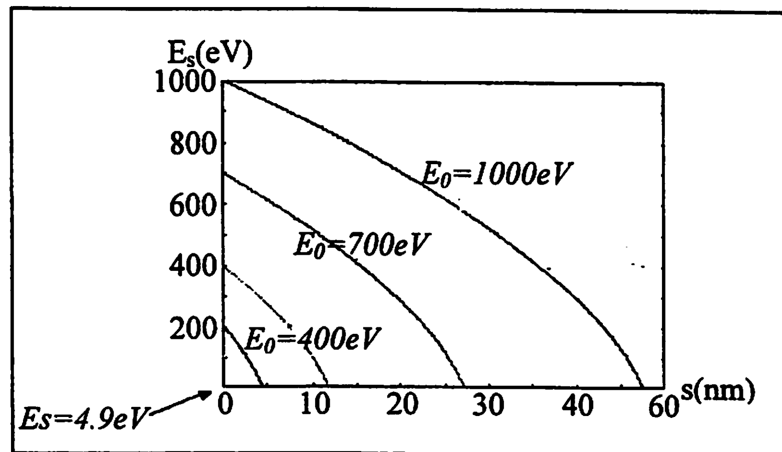

Figure 9-4. Energy losses of secondary electrons along

Because the energies of secondaries are much lower compared to that of the primaries, their emission angles are almost perpendicular to the primary electron trajectories [22]:

Equation 9-6

$$\sin^2(\varphi - \frac{\pi}{2}) = \frac{E_{se}/m_e c^2 + 2E_{se}/E_{pr}}{2 + E_{se}/m_e c^2} \cong 0$$
$$\varphi \cong \frac{\pi}{2}$$

where ϕ is the emission angle of an arbitrary secondary electron. The angular deflections of secondary electrons are neglected in the ERIM model due to their short path lengths.

9.3. Exposure process

Modeling of the exposure process is illustrated with the PMMA resist and yet the discussion can be extended to chemically amplified resists as long as the proper binding energy is used in the modeling. Figure 9-5 shows an incoming electron with energy E (*E>4.9eV*) inducing a scission event in the PMMA resist. Here, the incoming electron could be either a primary or a secondary electron. In the ERIM model, during the scission process, one of the electrons in a *C-C* bond is ionized and emitted with kinetic energy ΔE causing the *C-C* bond to break.

Equation 9-7

$$\sigma_{exp} \cong \begin{cases} \frac{5}{3} \cdot \frac{\pi e^4}{E} \cdot \frac{1}{\varepsilon_b}, (E >> \varepsilon_b) \\ \frac{\pi e^4}{E + 2\varepsilon_b} \cdot (\frac{5}{3\varepsilon_b} - \frac{1}{E} - \frac{2\varepsilon_b}{3E^2} + \frac{\ln \varepsilon_b - \ln E}{E + \varepsilon_b}), (otherwise) \end{cases}$$

Since a secondary electron emission is involved, Vriens cross section is used to calculate the scission cross section:

Equation 9-8

$$\sigma_{exp} \cong \begin{cases} \frac{5}{3}\cdot\frac{\pi e^4}{E}\cdot\frac{1}{\varepsilon_b}, (E >> \varepsilon_b) \\ \frac{\pi e^4}{E+2\varepsilon_b}\cdot(\frac{5}{3\varepsilon_b}-\frac{1}{E}-\frac{2\varepsilon_b}{3E^2}+\frac{\ln\varepsilon_b-\ln E}{E+\varepsilon_b}), (otherwise) \end{cases}$$

where ϵ_b is the C-C binding energy of $4.9eV$.

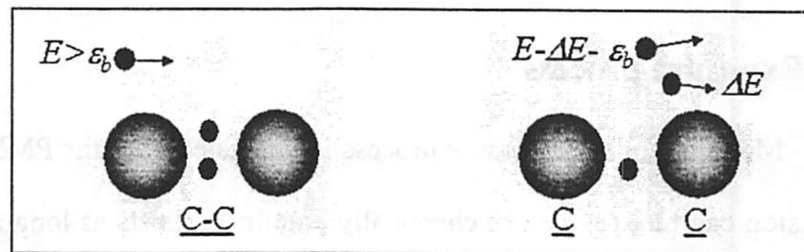

Figure 9-5. Schematic diagram of a scission event in PMMA.

Figure 9-6 shows how the exposure cross section changes with the electron energy E. The cross section is maximal when the electron energy is close to the C-C bond energy and decreases at large energies.

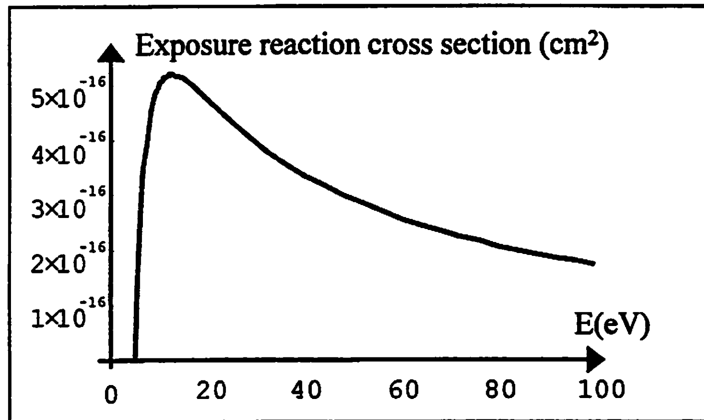

Figure 9-6. Electron energy dependency of the exposure cross section in PMMA.

The total number of scissions caused by the primary electrons is

Equation 9-9

$$N_{exp} = \sigma_{exp} \cdot n_c \cdot l \cdot 3000 = 43$$

where n_c is the backbone C-C bond density in PMMA and resist thickness $l=100nm$. Similar calculation shows that the number of scissions caused by the secondary electrons is around 180.

Clearly, the scission events are dominated by secondary electrons. Since the number of secondary electrons is inversely proportional to the primary electron energy, as presented in Section 9.2, the number of scission events also follows the inversely proportional relationship. Therefore, the exposure dose is proportional to the primary beam energy in the high-energy regime. This result agrees with experiments [75].

9.4. Spatial profile of exposure events

After the detailed investigation of secondary electron production and exposure mechanisms, we develop a formulation to describe the global distribution of the exposure events. The number of exposure events per unit distance along a secondary electron path can be evaluated based on the modified Bethe formula and the exposure cross section in the previous sections:

Equation 9-10

$$\sigma_{exp}\left[E_{se}\right]\cdot n_b = \sigma_{exp}\left[E_{se}(E_{so}, r)\right]\cdot n_b$$

$$where,\ \sigma_{exp} \cong \frac{\pi e^4}{E_{se}+2\varepsilon_b}\cdot\left(\frac{5}{3\varepsilon_b}-\frac{1}{E_{se}}-\frac{2\varepsilon_b}{3E_{se}^2}+\frac{\ln\varepsilon_b-\ln E_{se}}{E_{se}+\varepsilon_b}\right) \tag{8}$$

The number of secondary electrons emitted per unit energy is:

Equation 9-11

$$\frac{d\sigma_s}{dE_{so}}\cdot n_e \cong \frac{\pi e^4 n_e}{E_{pr}(E_{so}+J)^2} \tag{9}$$

Combining Equation 9-9 and Equation 9-10, one obtains the spatial distributions of the exposure events caused by the secondary electrons when a single primary electron incidents on the resist:

Equation 9-12

$$\tilde{f}_{exp}(r) = \int_{4.9eV}^{E_{pr}} \frac{\sigma_{exp}\left[E_{se}(E_{so}, r)\right]\cdot n_b}{2\pi r}\cdot n_e\cdot\frac{d\sigma_{so}}{dE_{so}}dE_{so}$$

If the deflections of primary electrons are taken into consideration, the above expression has to be convoluted with the spatial distribution of primary electrons:

Equation 9-13

$$f_{exp}(r) = \tilde{f}_{exp}(r) * f_{pr}(r)$$

9.6. Exposure dose

Equation 9-8 clearly shows how the exposure reaction cross section depends on binding energy ϵ_b. Meanwhile, the exposure cross section is proportional to the number of exposure events per unit volume if all other resist and beam parameters remain unchanged. Thus, the normalized number of exposure events per unit volume is plotted against binding energy ϵ_b for different electron energies in Figure 9-7.

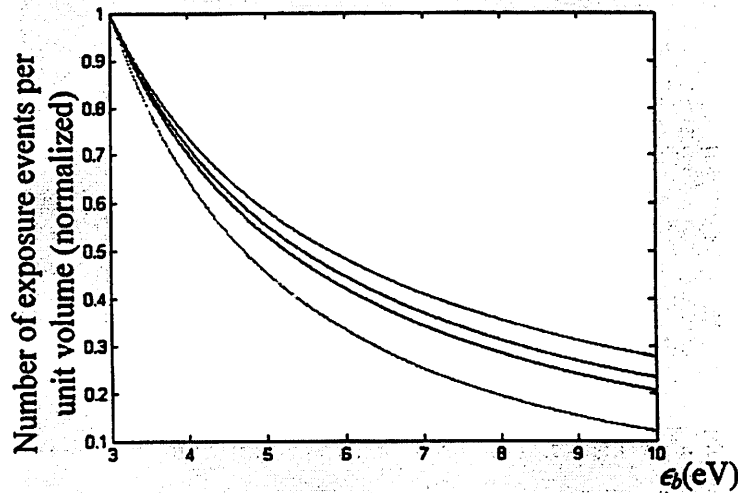

Figure 9-7. The normalized number of exposure events per unit volume against the binding energy ϵ_b at different electron energies E. From top to bottom, the curves correspond to $E=400eV$, $100eV$, $60eV$, and $20eV$, respectively.

As discussed in Section 9.2 and Section 9.3, the exposure reactions are dominated by the secondary electrons at energies of *400eV* or below. Figure 9-6 shows that at energy *E=400eV*, the number of exposures per unit volume is inversely proportional to binding energy ϵ_b if other resist and beam parameters remain unchanged. For energy below 400eV, the number of exposures decreases even faster. In order to maintain the minimum number of exposures per unit volume, one must increase the exposure dose and thus increase the number of secondary electrons. The exposure dose follows the conventional definition, which is the amount of charges incident on a unit area of the photo-resist. Therefore, the ERIM model predicts that the minimal exposure dose is a super-linear function of the binding energy ϵ_b. On the other hand, a larger binding energy will lead to smaller line width if the exposure dose is held constant. These results are beyond the framework of Murata's Hybrid model, which only considers total deposited energy rather than exposure cross sections.

9.7. Conclusions and discussion

An analytical electron resist interaction model ERIM has been developed to study the detailed mechanisms of the exposure events. It has been found that secondary electrons are responsible for up to *80%* of the exposure events. The model predicts that the minimum exposure dose ($\mu C/cm^2$) is proportional to the primary electron energy in the high-energy regime, which agrees with experiments. The ERIM model also predicts that the minimal exposure dose is a super-linear function of the binding energy for exposures if other resist and beam parameters remain unchanged. This result is still to be

confirmed in experiments. The above results are beyond the scope of the hybrid model developed by Murata, which only considers the total energy deposited in the resist.

An algebraic expression is derived for the spatial distribution of the exposure events. The expression is suitable for numerical solution. The ERIM model can be extended to chemically amplified resists by adjusting the binding energy.

There are still some open questions regarding the resist exposure process and the ERIM model. According to the prediction of the ERIM model, only around *22.3* exposure events occur in a $10nm \times 10nm \times 10nm$ volume of PMMA at the minimum exposure dose of $500 \mu C/cm^2$. The average spacing between adjacent exposures is 3.5nm. For chemically amplified resist, the minimum exposure dose is usually five times smaller and the spacing between adjacent exposures would be around 6nm. This inhomogeneity of exposures can be smoothed out during the post exposure bake.

Experimental results by Shultz [76] and Greeneich [77] show respectively *0.0169 scissions/eV* and *0.019 scissions/eV* in PMMA polymer. This number is roughly nine times as large as the prediction by ERIM. One possible explanation for the discrepancy is that the ERIM model so far only includes exposure events that are directly caused by electron interactions with the C-C bond in the main chain. As a matter of fact, primary and secondary electrons also interact with other chemical bonds in PMMA and produce different kinds of radicals. Shultz [76] [78], Alexander [79], and Kircher [80] suggest that some of these radicals can rupture the main chain by disproportionation, which may

explain the ease of PMMA backbone rupture. There is still no consensus on the detailed mechanisms. If all the exposures caused by the radicals were included, the total number of exposure events would be considerably larger than the number predicted by ERIM. Nevertheless, the basic approach of ERIM can be extended to include the effect of radicals. The main conclusions given earlier in this section would still be valid since the binding energies for the backbone scission and for the radical productions are roughly the same.

The accuracy of the ERIM model also depends on the accuracy of the physical models such as the modified Bethe formula by Joy and Luo at energies below 100eV when the exposure cross section is very large. Further investigations are required in order to explain the discrepancies and to improve the ERIM model.

10 Conclusions

10.0. Numerical and analytical tools

In this thesis, three simulation and analytical tools are developed to study the electron Coulomb interactions in beam columns and electron interactions with photo-resist.

The Berkeley Electron Beam Simulator (BEBS), developed by the author, is a software program used to simulate the electron interactions in beam columns. It employs adaptive Fast Multipole Method and parallel codes for efficient and rigorous calculation of Coulomb forces. It also uses continuous-force interpolation and adaptive time steps to speed up time iteration. BEBS provides a series of options specific for studying the mechanisms of beam blur production. All of these special options have been successfully used to produce the academic contribution of this thesis. As one of the options, BEBS enables the stochastic effect simulator using positrons in the beam column, which directly produce the stochastic blur on the target plane.

There are two versions of BEBS running on the Network of Workstations (NOW) and the Millennium Cluster, respectively. A typical 30μA current simulation in a 40cm long column takes about one hour with ten 500MHz processors. Compared with Munro's electron beam simulator that has 9 to 4 percent errors in force calculation at a beam current of 5 to 30μA, BEBS can achieve up to 4-digit accuracy in forces with 3 to 5 times longer simulation time.

In order to study the structure of stochastic Coulomb interactions, the author developed a novel approach that combines simulation techniques and algebraic analysis. It not only avoids the sophisticated algebra and approximations of a conventional analytical approach but also reveals the structure of stochastic Coulomb interactions in certain beam configurations. This new approach has been successfully applied to the analysis of a crossover configuration and a homocentric parallel beam.

The Berkeley Electron-Resist Interaction Model (ERIM) has been investigated as an analytical approach to study electron resist interaction mechanisms based on reaction cross sections. This model provides an algebraic expression for the spatial distribution of exposure events in the photo resist.

10.1. Mechanism studies and beam blur reductions

This thesis discusses different mechanisms that cause beam blur in beam columns and in photo-resist. Several potential techniques for blur reductions are also proposed.

Studies show that beam blur is mostly produced in the region around the crossover in a multi-emitter array system. Thus, any blur reduction technique only need to focus on its effect on this region. Meanwhile, the blur contributions caused by inter-beamlet electron interactions dominate over those caused by intra-beamlet electron interactions, especially at large convergence angles. Effective ways are still to be found to isolate and reduce the inter-beamlet blur contributions. The beam blur contributions from different beamlets can be combined on a root mean square basis.

Mechanism that causes stochastic blur is examined from different perspectives. Unlike the space charge blur, stochastic blurs can not be easily reduced with conventional optics. Further studies are required in order to fully utilize the structure of stochastic interactions for possible blur reductions.

Although the stochastic effect has long been observed, it has never been directly measured in experiments and or in simulations. The Stochastic Effect Simulator enables the direct measurement of stochastic blur and demonstrates the "stochastic limit" for any technique that reduces space charge blur only. Simulations show that in 4× demagnification electron beam systems, the stochastic blur is proportional to beam current raised to the power of 0.62, column length raised to the power of 1.27, beam convergence angle raised to the power of –0.9, emitter spacing raised to the power of –0.45, and beam voltage raised to the power of –2/3. The scaling exponent 0.62 for beam current roughly agrees with Jansen's prediction of 0.67. The blur size is independent of the beam energy spread ΔE when it is within 15eV. Scaling laws for space charge blurs

are also developed. The scaling exponents agree with Han's simulation and experimental results [3] [42].

Simulations are used to test the basic assumptions of Mkrtchyan's theory on electron stochastic interaction in a beam column: (1) consideration of nearest-neighbors only, and (2) a randomized length, over which interactions are correlated. Analysis of a basic crossover beam shows that interactions with multiple rather than nearest neighboring electrons almost immediately become the norm rather than the exception as proposed by Mkrtchyan. The simulation shows that the randomized correlation length is a function of the beam diameter and that correlated interactions occur at other axial positions due to symmetry with respect to the beam crossover. The randomized correlation length assumption of Mkrtchyan's theory needs modification to take the symmetry into consideration.

The structures of stochastic Coulomb interactions have been revealed both in probe-forming beams and in multi-spot projection electron beam columns. It has been demonstrated that in a crossover configuration where the beam angles are equal, the blur contribution is nearly constant along the column, very similar to a parallel beam. The structure of the stochastic Coulomb interactions also implies possibilities in the reduction of stochastic beam blurs.

Different techniques that reduce the space charge blurs have been explored in simulation with either neutralizing ions or lens aberrations introduced in the projection

lenses. Blur reductions of *24%* and *31%* have been respectively achieved with the above two schemes at $30\mu A$ beam current and $1.5mR$ illumination convergence angle. The percentage reductions are more pronounced at higher beam currents. Future experimental works are required to test these ideas in high throughput e-beam systems.

ERIM is a recommended approach to study the detailed process of the exposure events. It is shown that secondary electrons are responsible for up to *80%* of the exposure events. The model predicts that the exposure dose is proportional to the primary electron energy in the high-energy regime, which agrees with experimental results. An algebraic expression for the spatial distribution of the exposure events is derived and is suitable for numerical solution. The ERIM model also predicts that the minimal exposure dose is a super-linear function of the bond energy for exposure. The model can be potentially extended to chemically amplified resists through adjusting the binding energy.

10.2. Future work

The aberration compensation and beam neutralization techniques suggested in this thesis are subject to dynamic changes in projected pattern and pattern displacement. These effects can be viewed as transient effects and demand further investigations. For the space charge neutralization technique, the ion cloud reaches the optimal distribution during the transient period after the beam current changes. The introduced aberration also takes a transient period to reach its desired magnitude. The length of the transient time will directly influence the throughput of an e-beam system.

Even without these beam blur compensation techniques, there are a number of interesting transient questions, such as the resolution of the initial burst of electrons down the column. At present, e-beam systems suggest that these effects are, however, small compared to the overall exposures.

Simulations show about *30%* beam blur reduction at $30\mu A$ beam current in a 25-emitter array system with space charge blur reduction techniques. The blur size has been reduced from 88nm to around 60nm, which is close to the 56nm stochastic blur limit. The reduced spot size would satisfy the 70nm resolution requirement in high-throughput e-beam lithography. However, these results are based on either ideal ion distributions or ideal lens aberrations and the blur reductions would be smaller in experimental systems. The future work in this area should focus on the experimental implementation of these techniques.

The potential application of the structure of stochastic Coulomb interactions requires further investigations. The structure suggests the possibility of reducing stochastic blurs through manipulating the electron trajectories, which could improve the ultimate resolution of e-beam systems.

The ERIM model can be extended to chemically amplified resists by adjusting the binding energy. The accuracy of the model needs to be improved by including the indirect exposures through radicals and quantifying all the energy transfer pathways. Experimental work is required to test the relationship between the binding energy and the

minimal exposure dose, as predicted by ERIM. It will also be interesting to look at creation of exposure events when resist molecules are modeled as dipoles.

Bibliography

1. J.A. Liddle, S. D. Berger, "High throughput projection electron-beam lithography employing SCAPEL", *SPIE Proc*, vol. 2014 Charged-Particle Optics, 1993.
2. H.C. Pfeiffer *et al.*, "Projection reduction exposure with variable axis immersion lenses: Next generation lithography", *J. Vac. Sci. Technol. B*, Nov/Dec. 1999.
3. L. Han, W.D. Meisburger, R.F. Pease, G.I. Winograd, "The Global Space Charge Effects in High Throughput Electron Beam Lithography", *Private communication*, 1999.
4. S.T. Stanton, J.A. Liddle, W.K. Waskiewicz, M.M. Mkrtchyan, A.E. Novembre and L.R. Harriott, "Critical issues for developing a high-throughput SCALPEL system for sub-0.18 micron lithography generations", *SPIE Proc.* vol. 3331, pp.673, 1998.
5. D.F. Kyser and K. Murata, *Proc. Of the Sixth International Conference on Electron and Ion Beam Science and Technology* (Electrochemical Society, Priceton, N.J., 1974), pp. 205.
6. M. M. Mkrtchyan, J.A. Liddle and S.D. Berger, "Stochastic Scattering in Charged Particle Projection System: A Nearest Neighbor Approach", *J. Appl. Phys.* 78(12), pp. 6888, 1995.

7. G. H. Jansen, “Coulomb Interactions in Particle Beams”, *J. Vac. Sci. Technol. B*, Nov/Dec. 1988.

8. E. Munro and H.C. Chu, “Numerical analysis of electron beam lithography systems. I. Computation of fields in magnetic deflectors”, *Optik*, vol.60, no.4, p.371, March 1982.

9. E. Munro, “Electron and ion optical design software for integrated circuit manufacturing equipment”, *J. of Vacuum Sciences & Technology B*, vol. 15, pp.2692, 1997.

10. J. Barnes and P. Hut, “A Heirarchical O(NlogN) Force-Calculation Algorithm”, *Nature*, vol. 324, pp. 446-449, 1986.

11. E. Munro, “Simulation of discrete Coulomb interactions in high-current projection and multi-beam columns”, *SPIE Proc.* vol. 3777, Denver, 1999.

12. G. I. Winograd, “Space Charge Induced Aberrations”, *J. of Vacuum Sciences & Technology B*, vol. 17, pp.2803-07, 1999.

13. G. I. Winograd, *private communications,* 1999.

14. D.T. Blackston, J. Demmel, A.R. Neureuther and B. Wu, “On the Integration of an Adaptive Parallel N-Body Solver into a Particle by Particle Electron Beam Interaction Simulator”, *SPIE Proc.* vol. 3777, Denver, 1999.

15. B. Blackston, “Pbody: a parallel N-body library”, Ph.D. Thesis, University of California, Berkeley, May 2000.

16. J. Carrier, L. Greengard and V. Rokhlin, “A fast adaptive algorithm for particle simulations”, *SIAM J. on Sci. and Stat. Comp.*, vol.9, pp.669, 1988.

17. J. Singer, *The parallel fast multipole method in molecular dynamics*, Ph.D. Thesis, University of Houston, Aug. 1995.

18. B. Wu and A. R. Neureuther, "Structure of stochastic Coulomb interactions in electron beam columns", *J. Vac. Sci. Technol. B*, Nov/Dec. 2000.

19. J. S. Greeneich and T. Van Duzer, "An Approximate Formula for Electron Energy Versus Path Length", *IEEE Trans. on Electron Devices*, 1973.

20. J. S. Greeneich and T. Van Duzer, "An exposure model for electron sensitive resists", *IEEE Trans. on Electron Devices*, 1974.

21. R. Shimizu and T. E. Everhart, "Monte Carlo simulation of the energy dissipation of an electron beam in an organic specimen", *Optik*, vol. 36, pp.59, 1972.

22. K. Murata, "Monte Carlo simulation of electron scattering in resist film/substrate targets", Electron beam interaction with solids (AMF O'Hare, Chicago 1988), pp311.

23. K. Murata, M. Yasuda and H. Kawata, "Effects of the introduction of the descrete energy loss process into Monte Carlo Simulation of electron scattering", *Scanning*, vol. 17, pp. 228-234 (1995).

24. B. Wu and A. R. Neureuther, "Energy Deposition and Transfer in Electron Beam Lithography", *J. Vac. Sci. Technol. B*, Nov/Dec. 2001.

25. B. Wu and A. R. Neureuther, "Coulomb interactions and the effect of compensating lens aberration in projection electron-beam systems", *SPIE Proc.* vol. 3997, Santa Clara, 2000.

26. G.H. Jansen, "Trajectory displacement effect in particle projection lithography systems: modifications to the extended two-particle theory and Monte Carlo simulation technique", *J. of Applied Physics*, vol. 84, no. 8, pp. 4549-4567, 1998.

27. G. H. Jansen, *Coulomb Interactions in Particle Beams*, Academic Press, New York, 1990.

28. L.C. Chao, J. Orloff and L. Wang, *J. Vac. Sci. Technol.*, Vol.15, pp.2732, 1997.

29. J. Orloff, "Spherical aberration correction of a focused ion beam with space charge", *SPIE Proc.*, vol. 3155, pp.216, 1997.

30. K. Xiu, "Electron Optics Research on SCALPEL", *SRC Contract Review Task 629.001*, 2000.

31. K. Xiu, J.M. Gibson, "Correction of the field curvature in SCALPEL projection systems", *J. Vac. Sci. Technol. B*, Nov. 2000.

32. B. Wu and A. R. Neureuther, "Impact of positive ions and effect of lens aberrations in projection electron-beam systems", *SPIE Proc.* vol. 4343, Santa Clara, 2001.

33. S.D. Berger, D.J. Eaglesham, R.C. Farrow, R.R. Freeman, J.S. Kraus and J.A. Liddle, "Particle-particle interaction effects in image projection lithography systems", *J. Vac. Sci. Technol. B*, Nov/Dec. 1993.

34. W. Stickel, "Coulomb interactions in particle beam systems", *SPIE Proc.* vol.2522, San Diego, 1995.

35. D.F. Kyser, "Spatial resolution limits in electron beam nanolithography", *J. Vac. Sci. Technol. B*, Oct/Dec. 1983.

36. D.C. joy, "The spatial resolution limit of electron lithography", *Microelectronic Engineering 1*, pp.103-109, 1983.

37. A. Weidenhausen, R. Spehr and H. Rose, "Stochastic ray deflections in focused charged particle beams", *Optik*, vol. 69, no. 3, pp.126, 1985.

38. H. Rose and R. Spehr, "On the theory of the Boersch effect", *Optik*, vol. 57, no. 3, pp.339, 1980.

39. M. M. Mkrtchyan, J.A. Liddle, S.D. Berger, L.R. Harriot, A.V. Schwartz and J.M. Gibson, "An analytical model of stochastic interaction effects in projection systems using a nearest-neighbor approach", *J. Vac. Sci. Technol. B*, Nov/Dec. 1994.

40. J.M.J. van Leeuwen and G.H. Jansen, "Statistical limitations in electron beam lithography", *Optik*, vol. 65, no. 3, pp.179, 1983.

41. A.D. Brodie and W.D. Meisburger, "Conceptual models for understanding and minimizing Coulomb interactions", *Microelectronic Engineering*, vol17, pp.399, 1992.

42. L. Han, *private communications*, 1999.

43. J.A. Liddle, M.I. Blakey, C.S. Knurek, M.M. Mkrtchyan, A.E. Novembre, L. Ocola, T. Saunders and W.K. Waskiewicz, "Space-charge limitations to throughput in projection electron-beam lithography (SCALPEL)", *Microelectronic Engineering*, vol.41-42, pp.155, March 1998.

44. M. Mkrtchyan, J.A. Liddle, L.R. Harriott, E. Munro, "Space charge effects in e-beam projection lithography", *Solid State Technology*, vol.43, no.7, pp.241, July 2000.

45. J.B. Johnson, "A low voltage cathode ray oscillography", *J. Opt. Soc. Am.*, vol.6, pp.701, 1922.

46. E.G. Linder and K.G. Hernqvist, "Space charge effects in electron beams and their reduction by positive ion trapping", *J. Appl. Phys.*, vol21, pp.1088, 1950.

47. M.V. Nezlin, "Plasma instabilities and the compensation of space charge in an ion beam", *Plasma Phys.*, vol10, pp.337, 1968.

48. G.H. Jansen, "Fast Monte Carlo simulation of charged particle beams", *J. of Vacuum Sciences & Technology B*, vol.5, pp.146, Jan/Feb 1987.

49. A.R. Neureuther and O. Carmichael, "Computer Intensive Problems in Simulation of Integrated Circuit Lithography and Topography," *Proceedings of NASA Workshop*, pp. xxx, March 1996.

50. V.S.H. Wen, O.T. Carmichael, H. Yamashita and A.R. Neureuther, "Rigorous simulation of statistical electron-electron interactions with fast multipole acceleration and a network of workstations", *J. of Vacuum Sciences & Technology B*, vol. 16, pp.3221, 1998.

51. W.T. Rankin and J.B. Board Jr., "A portable distributed implementation of the parallel multi-pole tree algorithm", http://ftp.ee.duke.edu/pub/SciComp/papers/TR95-002.ps.Z, 1995

52. L. Reimer, H. Glide, "Monte Carlo rechnungen zur elektronen-diffusion", *Optik*, vol.27, pp.86, 1968.

53. H.A. Bethe and J. Ashkin, *Experimental Nuclear Physics,* vol. 1 (ed. by E. Segre, Wiley, New York, 1953), pp. 166-357.

54. L. Reimer, H. Glide and K.H. Sommer, "The broadening of an electron beam (17-2000keV by multiple scattering)", *Optik*, vol.30, pp.590, 1970.

55. L. Curgenven and P. Duncumb, "Simulation of electron trajectories in a solid target by a simple Monte Carlo technique", *Tube investments research report N. 303*, Saffron Walden, Essex, England, 1971.

56. K. Murata, T. Matsukawa R. Shimizu, "Monte Carlo calculations on electron scattering in a solid target", *Jpn. . Appl. Phys.* vol.10, pp.678, 1971.

57. R. Shimizu, T. Ikuta, T.E. Everhart, W.J. DeVore, "Experimental and theoretical study of energy dissipation profiles of keV electron in polymethyl methacrylate", *J. Appl. Phys.* vol.46, pp.1581, 1975.

58. K. Murata, D.F. Kyser and C.H. Ting, "Monte Carlo simulation of fast secondary electron production in electron beam resists", *J. Appl. Phys*, vol. 52, July 1981.

59. L. Vriens, *Proc. Phys. Soc.* vol. 89, pp.13-21, 1966.

60. D.C. Joy and S. Luo, "An empirical stopping power relationship for low-energy electrons", *Scanning*, vol. 11, pp.176-180, 1989.

61. M.I. Lutwyche, "The resolution of electron beam lithography", *Microelectronic Engineering*, vol.17, pp.17, 1992.

62. G. Han and F. Cerrina, "Energy transfer between electrons and photoresist: its relation to resolution", *J. Vac. Sci. Technol. B*, Nov/Dec. 2000.

63. http://now.cs.berkeley.edu.

64. http://www.millennium.berkeley.edu.

65. B. Blackston, "Pbody: a parallel N-body library", *Ph.D. Thesis*, University of California, Berkeley, pp.88, May 2000.

66. J.K. Salmon, "Skeletons from the treecode closet", *J. of Comp. Phys.*, March 1993.

67. B. Blackston, "Pbody: a parallel N-body library", *Ph.D. Thesis*, University of California, Berkeley, pp.39, May 2000.

68. F. Zhao, "An *O(N)* algorithm for three-dimensional N-body simulations", *Technical report*, Artificial intelligence lab, MIT, Cambridge, Oct. 1987.

69. E. Munro, *private communications*, 1999.

70. Griffiths, *Introduction to Electrodynamics (2nd Ed.)*, Prentice-Hall, Inc., pp.462, 1989.

71. Griffiths, *Introduction to Electrodynamics (2nd Ed.)*, Prentice-Hall, Inc., pp.487, 1989.

72. M. Born and E. Wolf, *Principle of optics: electromagnetic theory of propagation, interference and diffraction of light,* Cambridge University Press, 1999.

73. D. Malacara and Z. Malacara, *Handbook of lens design,* Marcel Dekker, 1994

74. D.C. Joy, *Monte Carlo Modeling for Electron Microscopy and Microanalysis* (Oxford University Press, 1995), pp.33.

75. J. Kedzierski, *private communications*, 2001.

76. A.R. Shultz, P.I. Roth and G.B. Rathmann, "Light scattering and viscosity study of electron-irradiation polystyrene and polymethacrylates", *J. of Poly. Sci.* vol. 35, pp369, 1956.

77. J.S. Greeneich, *Electron-beam technology in microelectronic fabrication*, Ed. by G. Brewer, Academic Press, Inc., 1980.

78. A.R. Shultz, "High energy radiation effects on polyacrylates and polymethacrylates", *J. of Poly. Sci.* vol. 22, pp.369, 1959.

79. P. Alexander, A. Charlesby, M. Ross, "The degradationof solid polymethylmethacrylate by ionizing radiation", *Proc. Roy. Soc. (London)*, vol.223, pp.392, 1954.

80. J.F. Kircher, F.A. Sliemers, R.A. Markle, W.B. Gager, and R.I. Leininger, "On the degradation and electron spin resonance spectra of irradiated methacrylate polymers", *J. Phys. Chem.*, vol.69, pp.189, 1965.